JGR Solid Earth

RESEARCH ARTICLE
10.1029/2023JB026593

Global Geomagnetic Field Evolution From 900 to 700 ka Including the Matuyama-Brunhes Reversal

Ahmed Nasser Mahgoub[1,2], **Monika Korte**[1], **and Sanja Panovska**[1]

[1]Helmholtz Centre Potsdam GFZ German Research Centre for Geosciences, Section 2.3 – Geomagnetism, Potsdam, Germany, [2]Geology Department, Assiut University, Assiut, Egypt

Key Points:

- A global geomagnetic field model for 900–700 ka is presented, including the Matuyama-Brunhes (MB) reversal and Kamikatsura excursion
- The mid-point of the Matuyama-Brunhes reversal is at 780 ka, with an overall duration of nearly 30 Kyr
- The dipole field decays from moderate dipole moment in the late Matuyama and recovers quickly to higher values in the early Brunhes

Supporting Information:

Supporting Information may be found in the online version of this article.

Correspondence to:

A. N. Mahgoub,
ahmedn@gfz-potsdam.de

Citation:

Mahgoub, A. N., Korte, M., & Panovska, S. (2023). Global geomagnetic field evolution from 900 to 700 ka including the Matuyama-Brunhes reversal. *Journal of Geophysical Research: Solid Earth*, *128*, e2023JB026593. https://doi.org/10.1029/2023JB026593

Received 21 FEB 2023
Accepted 25 MAY 2023

Author Contributions:

Conceptualization: Ahmed Nasser Mahgoub, Monika Korte, Sanja Panovska
Data curation: Ahmed Nasser Mahgoub, Sanja Panovska
Formal analysis: Ahmed Nasser Mahgoub, Sanja Panovska
Funding acquisition: Ahmed Nasser Mahgoub, Monika Korte
Investigation: Ahmed Nasser Mahgoub, Monika Korte, Sanja Panovska
Methodology: Ahmed Nasser Mahgoub, Monika Korte, Sanja Panovska
Project Administration: Ahmed Nasser Mahgoub, Monika Korte
Resources: Monika Korte

Abstract Polarity reversals and excursions are the most significant geomagnetic field changes generated in the liquid outer core of the Earth, therefore studying them helps understand geodynamo processes. This study examines the Matuyama-Brunhes (MB) reversal using a new reconstruction of the global geomagnetic field based on paleomagnetic data, termed Global Geomagnetic Field Model for the MB reversal (GGFMB). GGFMB covers 900–700 ka, including late Matuyama and early Brunhes. This allows us to also investigate the Kamikatsura excursion (ca. 888 ka). The model is based on 38 high-quality paleomagnetic sediment records with age control mostly independent of the magnetic signal. GGFMB suggests that the MB reversal began about ~799 ka, when non-dipole field components increased and the axial dipole component decreased. The transitional fields first appeared on Earth's surface in the high-latitude southern hemisphere and equatorial regions. The minimum dipole strength was reached around 780 ka and the axial dipole changed sign. After ~10 Kyr, the field stabilized in the normal polarity of the early Brunhes. The MB reversal lasted ~29 Kyr (from 799 to 770 ka) and had slower rate of dipole decay than recovery as well as lower dipole moment for several millennia before than after the reversal. According to GGFMB, the dipole moment during the Kamikatsura excursion was approximately half that of the current field and it was a regional excursion observed only over eastern Asia and North America. Our sediment data collection is heavily biased toward the northern hemisphere, thus more southern hemisphere records are needed to demonstrate GGFMB's robustness in this region.

Plain Language Summary The Earth's magnetic field originates deep inside the planet and extends far into space, and it has undergone significant direction and intensity changes throughout geological history. The most extreme magnetic field changes are reversals, when the field changes its polarity and global field intensity reaches a minimum. We reconstruct the global geomagnetic field evolution over the time interval 900,000 to 700,000 years ago. The information about the magnetic field variations comes from the paleomagnetic signal recovered from sediment drill cores from locations all over the globe, and with good constraints on the ages of the material. Our model includes the Matuyama-Brunhes field reversal, which occurred ~780,000 years ago. It provides a global view of this drastic field change, indicating, for example, that the recovery of the global field intensity was much faster than its decay and the average global field strength was lower for several millennia before than after the polarity change. Our model suggests that the reversal started at ~799 ka, the actual polarity change of the axial dipole field occurred at ~780 ka, and a stable normal polarity was reached at ~770 ka. The whole process of the reversal therefore took ~29,000 years.

1. Introduction

The geomagnetic field is produced by dynamo processes in Earth's outer fluid core, and its continuous change in time and space is known as secular variation (Aubert et al., 2013; Backus et al., 1996; Merrill & McFadden, 1999). Most of the time the field is dominated by a nearly geocentric axial dipole geometry. However, occasionally it undergoes dramatic changes known as reversals and excursions (e.g., Channell et al., 2020; Laj & Channell, 2015; Merrill & McFadden, 1999; Roberts, 2008), when the field geometry significantly departs from the axial dipole and even reverses, and the intensity reaches its lowest levels (Dagley & Lawley, 1974; Guyodo & Valet, 1999; Lawley, 1970; Singer, 2014; Valet & Fournier, 2016; Van Zijl et al., 1962; Verosub & Banerjee, 1977). In the case of an excursion, the field returns to its original polarity after a few thousand years, and strong deviations from the axial dipole geometry are not always globally noted. During a reversal, the field completely changes polarity, with stable dipole dominated phases of opposite polarity before and after. A global understanding of the characteristics of these events is crucial to fully understand the underlying geodynamo

Software: Ahmed Nasser Mahgoub, Monika Korte, Sanja Panovska
Supervision: Monika Korte
Validation: Ahmed Nasser Mahgoub, Monika Korte, Sanja Panovska
Visualization: Ahmed Nasser Mahgoub, Monika Korte, Sanja Panovska
Writing – original draft: Ahmed Nasser Mahgoub
Writing – review & editing: Ahmed Nasser Mahgoub, Monika Korte, Sanja Panovska

processes (Glatzmaiers & Roberts, 1995; Olson et al., 2011). The Matuyama-Brunhes (MB), the most recent field reversal, offers an excellent opportunity to comprehend reversal mechanisms (Amit et al., 2010; Olson et al., 2011).

The primary sources of information for reversals and excursions are paleomagnetic data records, obtained mainly from lava flows and sediment cores. Thermal remanent magnetization (TRM) acquisition in lavas has a well-established theoretical background (Néel, 1955). Also, lavas often have more stable magnetic signals than sediments do. However, lava records are scarce and discrete, and thus not sufficient to fully describe reversals or excursions. Sediment drill cores offer a much better spatial and temporal coverage of paleomagnetic field evolution by providing continuous records of depositional and post-depositional remanent magnetization (PDRM). However, several concerns [including signal smoothing (Lund & Keigwin, 1994), potential inclination shallowing (Arason & Levi, 1990; Deamer & Kodama, 1990), and lock-in depth (Channell et al., 2004; Lund & Keigwin, 1994; Sagnotti et al., 2005)] about the efficiency of sediment records to reliably capture fast magnetic field changes have to be kept in mind (see Roberts & Winklhofer, 2004; Valet & Fournier, 2016).

The timing and duration of the MB reversal are still debated (see e.g., Channell et al., 2020), despite the fact that it is reasonably well covered by paleomagnetic data globally (in comparison to older field reversals). The two most commonly given ages are 773 ka (Channell et al., 2010; Jouzel et al., 2007; Raisbeck et al., 2006; Singer et al., 2019; Valet et al., 2014) and 780 ka (Shackleton et al., 1990). The proposed duration ranges from 1 to 10 Kyr (e.g., Clement, 2004; Singer et al., 2005), to recently proposed ∼22 Kyr (Singer et al., 2019). The latter was proposed from an integration of paleomagnetic data of lavas and sediment records, and cosmogenic isotope production rates recorded by ice records, which increase during the time of low geomagnetic field intensity. It is based on both field direction and intensity, while earlier duration estimates were generally determined based only on directional data. A suitable tool to estimate age and duration of reversals and excursions from the full field vector is the paleosecular variation index (P_i), proposed by Panovska and Constable (2017). The index evaluates the departure of the virtual geomagnetic pole (VGP) latitude and virtual dipole moment (VDM) from the geographic pole and the present day dipole moment strength, respectively. With this (somewhat arbitrary) normalization relative to the present-day field, values above 0.5 for this dimensionless index are deemed indicative of transitional field. Mahgoub et al. (2023) used the P_i data of 20 global sediment records and deduced that the MB reversal evolved over a ∼30 Kyr time span, from 800 to 770 ka. Hartl and Tauxe (1996) discovered a period of decrease in paleointensity (DIP) at ∼795 ka, and considered it to be a precursor. This MB-precursor was subsequently documented in several sediment (e.g., Channell et al., 2004; Korff et al., 2016; Sagnotti et al., 2014; Valet et al., 2014) and lava (Singer et al., 2019; Valet et al., 2012) records, where the DIP was accompanied by transitional magnetic field directions (VGP latitude lying between +45° and −45°). Following the main polarity transition, Valet et al. (2012) observed another unstable geomagnetic phase with low-latitude VGPs, which they called a rebound. In comparison to the precursor, the rebound was documented in much fewer records (Mahgoub et al., 2023; Singer et al., 2019).

Spherical harmonic (SH) global field models for the MB reversal were constructed previously (Ingham & Turner, 2008; Leonhardt & Fabian, 2007; Shao et al., 1999). Leonhardt and Fabian (2007) applied an iterative Bayesian inversion to create the IMMAB4 model, for the time interval of 794 to 764 ka, using four full vector data records. An inverse model is initially created from one record and then utilized to predict magnetic field data from a second input record. After correlation and time scale adjustment, the first and second data records are inverted again. The final model is created by repeating this method for the third and fourth records. Ingham and Turner (2008) constructed a model (named IT08 in the following) up to SH degree 3, using 11 records. The VGP latitude data of these records were utilized to align them on a common relative time scale, consisting of 39 discrete time steps spanning 31.5 Kyr. We note that IMMAB4 and IT08 models were thus not derived from records with independent dates.

In this study, a new global geomagnetic field model for the MB reversal (GGFMB) is established. Spanning the interval 900–700 ka, it also covers the late Matuyama chron with the Kamikatsura excursion (ca. 888 ka) and the early phase of the Brunhes. The input data for our reconstruction are described in Section 2. The modeling methodology is presented in Section 3. The results of our new model are presented in Section 4, including the fit to the data, the evolution of the magnetic field, and characteristics of the MB reversal in terms of field morphology and variation of reversal duration with latitude and longitude. Field morphology and time and duration of the Kamikatsura excursion are also discussed there.

2. Input Data

Mahgoub et al. (2023) compiled and carefully evaluated 68 sediment records for the interval 900–700 ka. Of these records, 56 are from deep-sea sediments and the remaining 12 are from shallow-sea and lake sediments. Only independently well-dated records with reasonable regional consistency in paleomagnetic directions and/or intensity (when several records from a region exist) were accepted for further analysis in our model. Thus, we use 38 out of the 68 records. Note that all updates on the original age scales of the records were taken into account. For more details on the data see Mahgoub et al. (2023). Table 1 contains a list of these records and the geographic distribution is shown in Figure 1a. The data distributions of the previous models IMMAB4 and IT08 are also shown there. The four IMMAB4 records are clearly all located in a narrow longitudinal band and along the Atlantic. The IT08 model has better spatial distribution, but our new data compilation clearly fills some further gaps. We expect to get a more representative model for global features of the geomagnetic field during MB reversal, but it should be noted that high quality, independently dated southern hemisphere records are still sparse and our data set is clearly biased toward the northern hemisphere. The North Atlantic records account for 70% of the total data set, 9% come from the Western equatorial Pacific, and 5% from the North Pacific, and all other regions comprise the remaining 16% of the whole data set. Moreover, the amount of data is highest around the MB reversal, between 800 and 760 ka (Figure 1b). Only the North Atlantic is covered homogeneously for the full 900–700 ka interval (Mahgoub et al., 2023).

From the 38 accepted records, 17 have full vector paleomagnetic data, 15 have only relative paleointensity (RPI), and 6 records have one or two magnetic field components. In total, 42,342 data points are available, distributed as follows: 12,442 declination, 12,894 inclination, and 17,006 RPI data points. Sediment RPI records do not provide information on absolute field intensity, and the PADM2M axial dipole moment model (Ziegler et al., 2011) was used to calibrate the RPI records to absolute values (for details see Mahgoub et al., 2023). Similarly, declination records often initially have no absolute azimuthal orientation and were checked, and if necessary adjusted to the common assumption of an average axial dipole field (i.e., average of 0° or 180° for normal or reverse polarity field), see Mahgoub et al. (2023).

Regarding temporal resolution, the sedimentation rate (SR) of the input records (Table 1) ranges from 0.5 to 89 cm/Kyr, with 22 records having SR $<$ 5 cm/Kyr; 3 in the range 5–10 cm/Kyr; and 13 records having SR $\geq$ 10 cm/Kyr. North Pacific records have the highest SR, and the maximum SR values of 89 cm/Kyr are found in three North Pacific shallow marine-records. Very good SRs, in the range of 25–60 cm/Kyr, are also found in the Mediterranean records. The North Atlantic records have semi-uniformly high SRs, mostly around $\geq$10 cm/Kyr. The data from the Western equatorial Pacific, on the other hand, show the lowest SRs. Similar results were obtained from a smoothing spline analysis following Panovska et al. (2012), which gives the smoothing time (Ts), that is, the time that can be resolved in a sediment record. Mahgoub et al. (2023) determined Ts ranges from 0.2 to 18.8 ka for the accepted records (included in Table 1) and concluded that ~50% of the input records can capture magnetic field behavior with a resolution better than 1 Kyr.

3. Methods

3.1. Modeling Procedure

Global geomagnetic field models (e.g., Constable et al., 2016; Korte et al., 2009; Panovska et al., 2018, 2021) are constructed by using the method described by Bloxham and Jackson (1992) and Jackson et al. (2000). A temporally continuous field model is constructed by using spherical harmonic basis functions in space and cubic B splines in time. The mantle is considered insulating (Benton & Whaler, 1983) and crustal and exterior magnetic fields are neglected. The time-dependent vector magnetic core field B(t) then can be written as the negative gradient of a scalar potential V(t); $B(t) = -\nabla V(t)$, which is expanded as

$$V(r,\theta,\phi,t) = a\sum_{l=1}^{l_{\max}}\sum_{m=0}^{l}\sum_{n=1}^{n_{\max}}(a/r)^{l+1}\left[g_l^{m,n}\cos(m\phi)+h_l^{m,n}\sin(m\phi)\right]P_l^m(\cos\theta)M_n(t), \quad (1)$$

where (r, θ, ϕ) are spherical polar coordinates, a = 6,371.2 km is Earth's mean radius and the $P_l^m(\cos\theta)$ are Schmidt quasi-normalized associated Legendre functions of degree l and order m. Standard time-dependent Gauss coefficients (g_l^m, h_l^m) are determined by cubic B-splines:

$$g_l^m(t) = \sum_{n=1}^{n_{\max}} g_l^{m,n} M_n(t)$$

Table 1
List of the 38 Sediment Cores Used to Construct the GGFMB Model

Record	Region	Lat. (°N)	Long. (°E)	SR (cm/Kyr)	Ts (Kyr)	Field comp.	References
U1306	N. Atlantic	58.24	−45.64	15.0	0.3	D/I/F	Channell et al. (2014)
U1307	N. Atlantic	58.51	−46.40	5.5	0.5	D/I/F	Mazaud et al. (2015)
U1308	N. Atlantic	49.90	−24.20	7.3	0.3	D/I/F	Channell et al. (2008)
ODP 983	N. Atlantic	60.40	−23.60	11.3	0.3	D/I/F	Channell et al. (1998, 2004) and Channell and Kleiven (2000)
ODP 984	N. Atlantic	61.40	−24.01	12.0	0.3	D/I/F	Channell et al. (2004)
ODP 980	N. Atlantic	55.50	−14.70	16.0	0.3	D/I/F	Channell and Raymo (2003)
ODP 769A	W. Eq. Pacific	8.80	121.30	10.0	0.2	D/I/F	Oda et al. (2000)
MD97-2143	W. Eq. Pacific	15.90	124.70	2.0	4.3	D/I/F	Horng et al. (2002, 2003)
OB	N. Pacific	34.80	135.60	60.0	0.6	D/I/F	Hyodo et al. (2006), Hyodo and Kitaba (2015), and Maegakiuchi et al. (2016)
YT	N. Pacific	35.30	140.10	89.0	1.6	D/I/F	Haneda et al. (2020)
CHBC	N. Pacific	35.30	140.10	89.0	0.7	D/I/F	Haneda et al. (2020)
CHBT	N. Pacific	35.38	140.31	18–30	0.6	D/I/F	Oda et al. (2022)
CADO	Antarctica	−64.90	144.80	4.4	1.1	D/I/F	Macrì et al. (2010)
HS	Mediterranean	39.31	16.34	35.0	0.3	D/I/F	Sagnotti et al. (2014, 2016)
MD90-0940	Eq. Indian Ocean	−5.60	61.70	1.3	2.6	D/I/F	Meynadier et al. (1994)
MD90-961	Eq. Indian Ocean	5.10	73.90	4.8	0.6	D/I/F	Valet et al. (2014)
CASA	Caribbean Sea	15.10	−59.60	1.7	18.8	D/I/F	Bieber et al. (2021)
U1304	N. Atlantic	53.10	−33.53	15.0	0.3	I/F	Xuan et al. (2016)
YGC	N. Pacific	35.40	140.10	89.0	0.4	D/I	Suganuma et al. (2015)
CB	Mediterranean	39.31	16.34	27–94	0.8	D/I	Macrì et al. (2018)
SO202-1	N. Pacific	38.00	164.50	2.1	7.7	I/F	Korff et al. (2016)
PC20	Antarctica	−65.00	143.80	0.6	5.3	I/F	Macrì et al. (2005)
ICDP-5011	Russian Arctic	67.50	172.00	4–5	1.1	I	Nowaczyk et al. (2013)
MD95-2016	N. Atlantic	57.40	−30.80	4.0	0.3	F	Valet et al. (2019)
KH73-4-7	W. Eq. Pacific	7.70	164.80	1.0	3.9	F	Sato and Kobayashi (1989)
KH73-4-8	W. Eq. Pacific	−1.60	167.60	1.0	4.3	F	Sato and Kobayashi (1989)
KH90-3-5	W. Eq. Pacific	4.00	160.00	1.0	7.1	F	Sato et al. (1998)
MD98-2183	W. Eq. Pacific	2.00	135.0	2.0	0.7	F	Yamazaki and Oda (2005)
MD98-2185	W. Eq. Pacific	3.10	135.00	2.0	4.6	F	Yamazaki and Oda (2005)
MD98-2187	W. Eq. Pacific	4.30	134.80	1.0	8.5	F	Yamazaki and Oda (2005)
KR0310-PC1	N. Pacific	35.20	175.00	1.2	7.3	F	Yamazaki and Kanamatsu (2007)
NPGP1401-2A	N. Pacific	32.00	178.60	0.7	15.6	F	Shin et al. (2019)
1101	Antarctica	−64.40	−70.30	8.8	1.0	F	Guyodo et al. (2001)
ODP 1010	E. N. Pacific	30.00	−118.10	1.3	1.7	F	Hayashida et al. (1999) and Leonhardt et al. (2009)
ODP 1021.A	E. N. Pacific	39.10	−126.20	4.0	1.9	F	Guyodo and Valet (1999) and Leonhardt et al. (2009)
LC07	Mediterranean	38.20	10.10	2.3	0.6	F	Dinarès-Turell et al. (2002)
MD90-949	Eq. Indian Ocean	2.10	76.10	2.8	1.8	F	Valet et al. (2016, 2019)
ODP 848-851	E. Eq. Pacific	2.00	−110.00	2.0	1.2	F	Valet and Meynadier (1993)

Note. Lat, latitude; Long, longitude; SR, sedimentation rate, Ts, smoothing time; D/I/F, declination/inclination/intensity—components of the magnetic field.

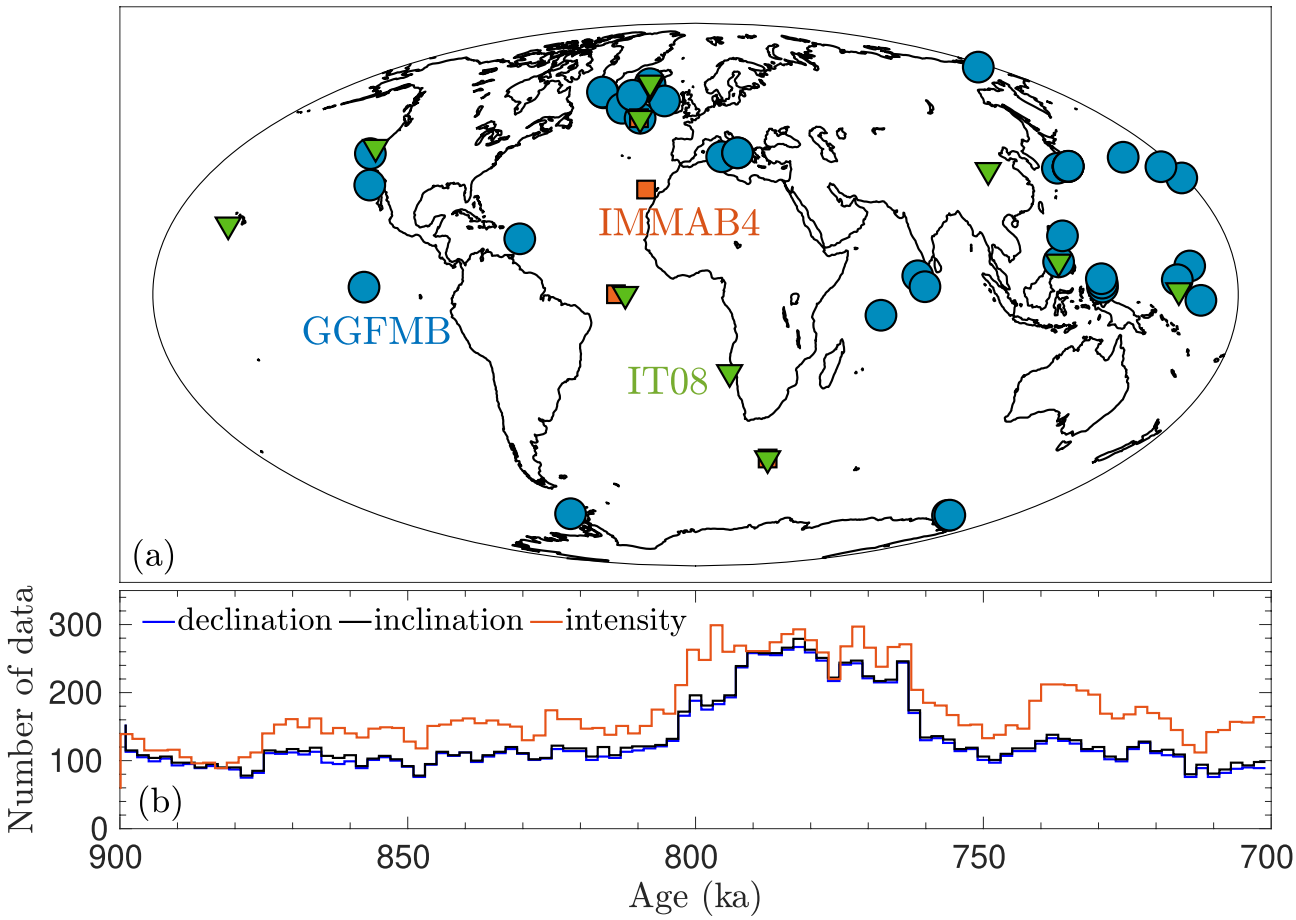

Figure 1. (a) Geographic distribution of sediment records used for SH models of the MB reversal. For the model of this study, GGFMB, 38 sediment records indicated by blue circles have been used. The orange squares refer to the 4 sites used in IMMAB4 model (Leonhardt & Fabian, 2007), and the green triangles to the 11 sites of the IT08 model (Ingham & Turner, 2008) (two sites at 60°N are at nearly the same location). (b) Temporal distributions of the declination, inclination, and intensity data of the GGFMB input records.

and similarly for h_i^m. Cubic B-splines are piecewise cubic polynomials, which form a basis of minimal support (De Boor, 2001). The ith cubic B-spline M_i becomes non-zero ($M_i(t) > 0$) only when t falls within the interval (t_i, t_{i+4}) of knot points t_n, $n = 1$ to n_{max}.

In order to determine the amount of structure in the model from the data, not the SH truncation degree, without overfitting the data given their uncertainties, we apply a regularization. Following Whaler and Gubbins (1981) and Gubbins (1983) both the misfit to the data and the amount of spatial and temporal structure in the model are minimized in form of the following expression:

$$(\gamma - fm)^t C_e^{-1}(\gamma - fm) + \lambda_S \psi(m) + \lambda_T \phi(m)$$

where $(\gamma - fm)$ is the error vector resulting from the difference between the data γ and the model (m) prediction, C_e^{-1} is the data error covariance matrix, and f is the operator connecting the data vector to the model. λ_S and λ_T are the damping parameters determining the trade-off between the misfit and the spatial (ψ) and temporal (ϕ) complexity of the model. We follow the approach as used for previous paleomagnetic field models, such as the series of Holocene CALSxk models (e.g., Constable et al., 2016; Korte et al., 2009), or the GGFSS70 (Panovska et al., 2021) and the GGF100 ka model of Panovska et al. (2018). As done there, we employed the minimal Ohmic heating norm described by Gubbins (1975) for spatial, and the second time derivative of the radial magnetic field integrated over the core-mantle boundary for temporal regularization. A linearization is needed for paleomagnetic directional and intensity data, which are non-linearly related to the coefficients. This was done by using a constant axial dipole $g_1^0 = -30$ μT as a starting model for the Gauss coefficients, and 20 iterations were performed

to reach to the final model. Note that the solution is independent of the starting model and convergence was reached in the 10^{th} iteration.

3.2. Modeling the MB Field Reversal

GGFMB is constructed using the approach described above with SH maximum degree (l_{max}) 6 and a 200 years knot point spacing. Unlike TRM data given from volcanic records, paleomagnetic data of sediment records are commonly provided without uncertainty estimates. TRM data uncertainties are commonly expressed in terms of α_{95}, which is the radius of the 95% confidence circle about the calculated mean direction (Fisher, 1953), and standard deviation for the intensity measurements (F), from averaging a number of individual sample results. Unfortunately, there is no way to define such uncertainty estimates for individual sediment records. Their actual uncertainties depend for example, on sampling, measuring techniques, and interpreting PDRM data. For RPI they also depend on how well the normalization eliminates influences from factors such as climate or grain size. These sources of errors are not easily checked nor corrected during the compilation of published sediment data (Mahgoub et al., 2023). We weight all sediment records equally by assigning them an α_{95} of 8.5° for directions and an uncertainty of 5 μT for calibrated RPI. The α_{95} is converted to standard deviation by using Suttie and Nilsson (2019) equations, with a note that declination standard deviation is dependent on inclination, which are steep at various locations during magnetic field instability periods, that is, excursions and reversals. Therefore, the standard deviation of declination was calculated using inclination values, estimated from a geocentric axial dipole: $\tan I = 2\tan\lambda$ where I is inclination and λ is site latitude. The inclination data then has a constant standard deviation of 3.4° while the declination standard deviation estimates depend on latitude.

The spatial (λ_S) and temporal (λ_T) regularization parameters were determined from trade-off curves (Panovska et al., 2018, 2021). For λ_S and λ_T values around the knee of the curves, we check properties of several models in terms of Gauss coefficients and fit to data. We strive for a model with a reasonable fit to the data (See 4.1), while avoiding models that fit the data too closely considering that their uncertainties are not well defined, as discussed above, and that we do not consider age uncertainties. Such models would likely include implausible small-scale structures. This process of choosing our preferred model (GGFMB) is somewhat subjective, but note that the models around the knee of the trade-off curve tend to show rather similar characteristics. The trade-off curves and our final choices of λ_S and λ_T are shown in Figure S1 in Supporting Information S1.

Iterative data rejection at different standard deviation (σ) levels (5σ, 10σ, and 20σ) during the inversion was tried. Using a 5σ level removes 9.9% of the total data: 1352 declination, 1417 inclination, and 1421 intensity values out of a total of 42,342 data get rejected. Rejection at 10σ level results in 496 declination, 462 inclination, and 84 intensity values, or 2.5% of the total data being rejected. 1.0% of data—206 declination, 247 inclination, and zero intensity—were rejected at 20σ. As the data rejection mainly occurs within the 800–750 ka interval around the MB reversal, when it is not unlikely that regionally different, strong and fast (directional) field variations cannot be fully captured by the regularized model, we decided on using the moderate rejection level of 10σ. The distributions of the rejected data (at 10σ level) are shown in Figure S2 in Supporting Information S1.

4. Results and Discussion

4.1. Fit to Data

The root mean square (RMS) misfit of the resultant GGFMB model normalized by the data uncertainty estimates is 2.4, while the average RMS misfit to the declination, inclination, and intensity data are comparable, with values of 2.4, 2.5, and 2.6, respectively. Histogram distributions of the normalized misfits are shown in Figure S3 in Supporting Information S1. The distributions are generally symmetric, but the intensity has a slight positive bias, indicating that the GGFMB model predictions tend to be on average slightly lower than the observed data.

Representative examples of declination, inclination, and intensity predictions from GGFMB for six sediment records are shown in Figure 2. Figures S4–S41 in Supporting Information S1 show the predictions for all components of each individual accepted record. Predictions from the earlier IMMAB4 model are included for comparison in Figure 2. GGFMB predicts the magnetic field components of most of the accepted records reasonably well. It cannot fully fit fast variations in high resolution records (e.g., Figures 2a and 2c or Figure S9 in Supporting Information S1), and has somewhat more variability than some low-resolution records (e.g., Figure S19 in

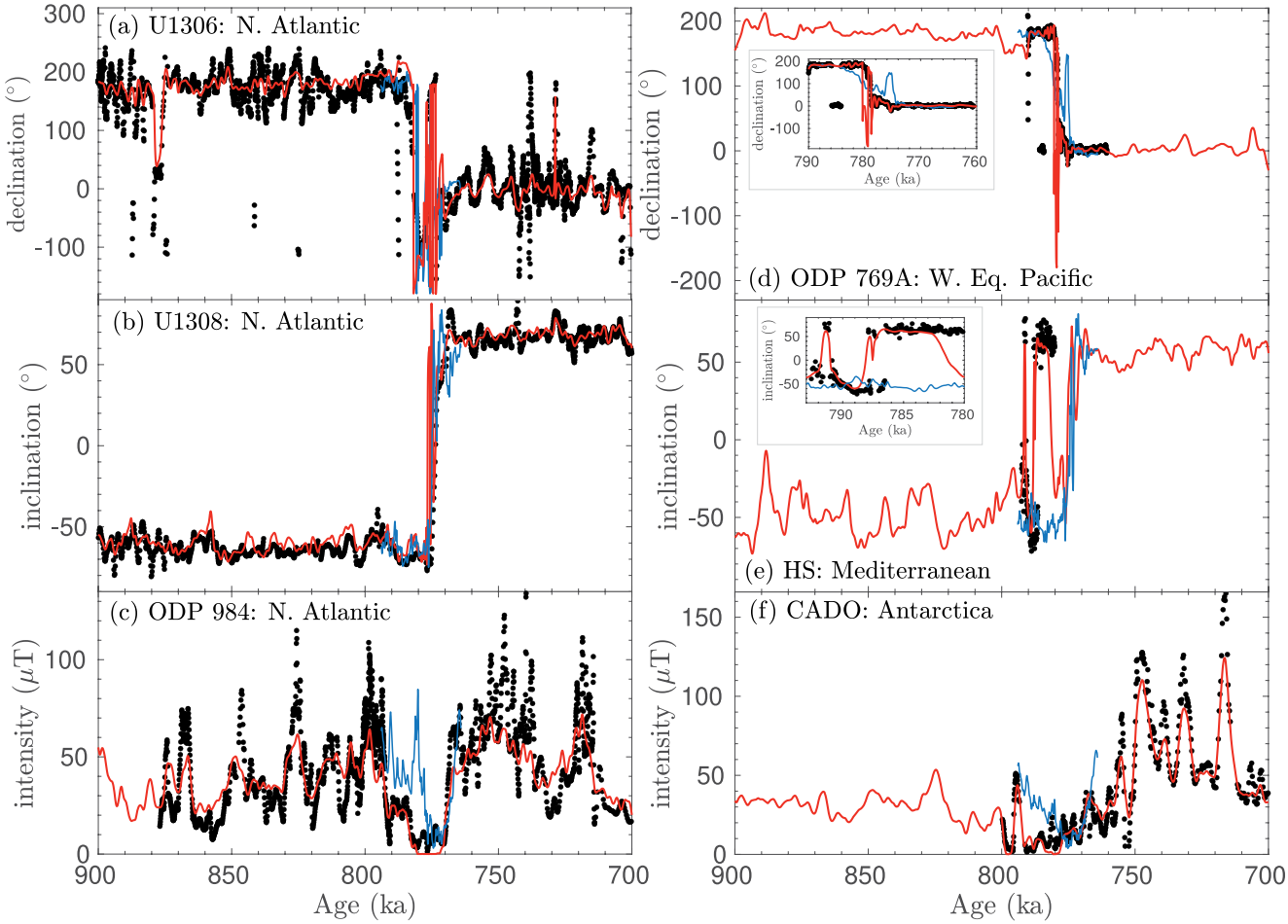

Figure 2. GGFMB model prediction (red lines) for declination (top), inclination (middle), and intensity (bottom) data of six different sediment records (black dots) that were used for creating the model. IMMAB4 model predictions (light blue lines) are shown for comparison. Insets d and e illustrate predictions of GGFMB and IMMAB4 for the time intervals covered by ODP769A (790–760 ka) and HS (793–780 ka), respectively.

Supporting Information S1). Some individual features, such as for example, a strong variation in the North Pacific around 815 ka (Figure S24 in Supporting Information S1), seem supported by rather few data (Figures S26 and S31 in Supporting Information S1) and should be interpreted with caution. Overall, however, the GGFMB model can be regarded as a reasonable global representation for magnetic field changes over the past 900–700 ka. Our new model has better prediction for most of the input records than IMMAB4 (Figure 2c–2f). In particular, the IMMAB4 intensity predictions in many cases have low values only for a narrower time interval (e.g., OPD 984 and CADO in Figures 2c and 2f, respectively) and do not fit low intensity data around 775–795 ka. IMMAB4 also in some cases predicts the main directional change at different times than suggested by our data compilation and fit by GGFMB, as seen for example, in inclination record HS in Figure 2e or the directional changes in record YGC in Figure S22 in Supporting Information S1.

To test the model, we compared GGFMB predictions to an independent data set (not used for model creation), using TRM data from lava flows. Mahgoub et al. (2023) compiled paleomagnetic lava results from 108 sites from eleven regions, spanning the interval 900–700 ka and having $^{40}Ar/^{39}Ar$ or K-Ar ages. For information on paleomagnetic data and ages of lavas sites, as well as citations, see Mahgoub et al. (2023). Figure 3 depicts the GGFMB predictions for Hawaii and Chile, while Figures S42–S50 in Supporting Information S1 show the predictions for the remaining regions. With the exception of a few paleointensity data whose values are less than model prediction values, there is a reasonable consistency between model predictions and the TRM data of Hawaii and Chile can be noted (Figure 3). This is generally true for the remaining lava regions, with the exception of a few individual data points (See Figures S47, S48, and S50 in Supporting Information S1). This general agreement with independent directional and absolute paleointensity data confirms the performance of GGFMB.

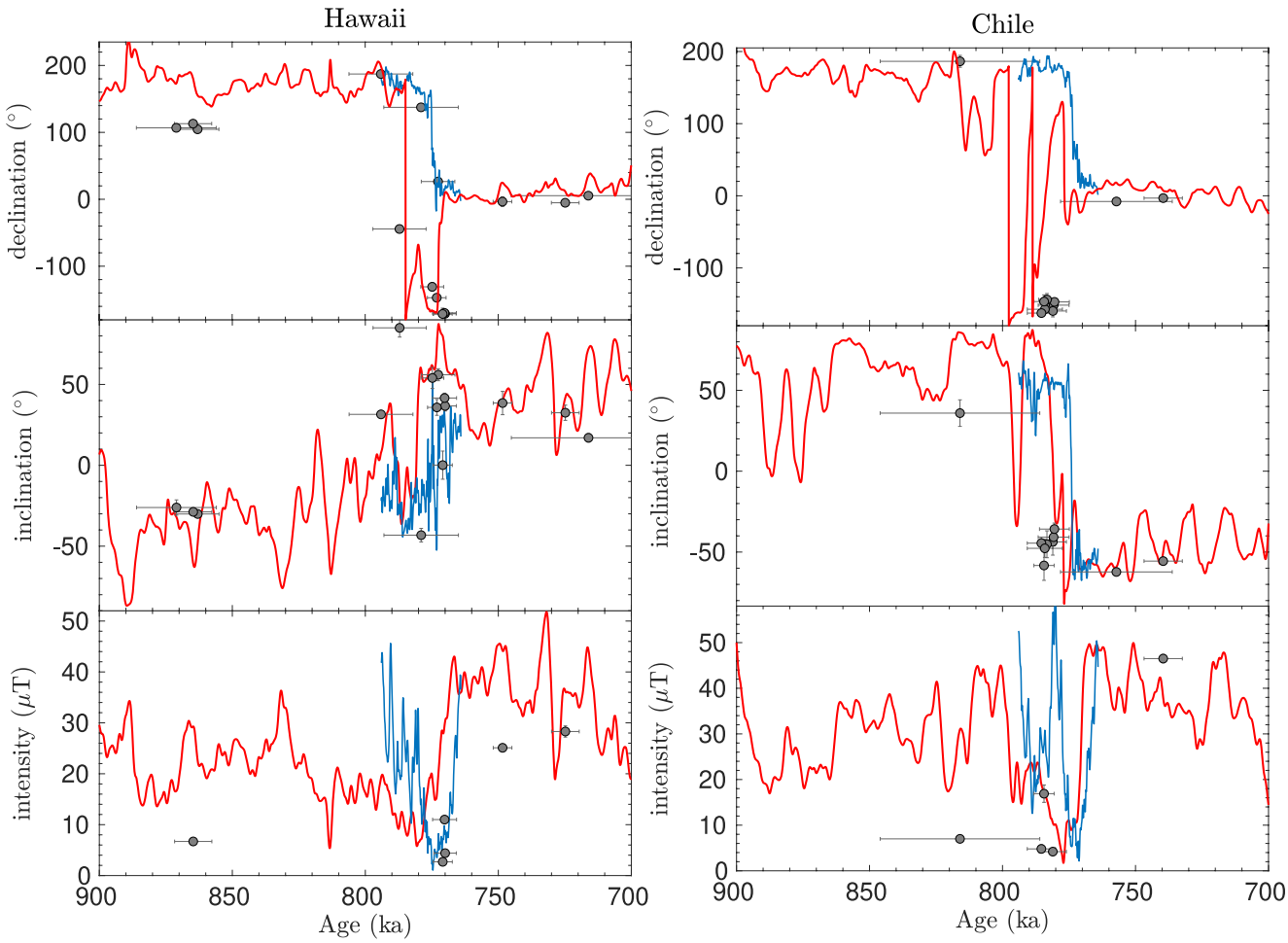

Figure 3. GGFMB model prediction (red lines) for paleomagnetic data from lavas (black dots) of Hawaii and Chile. IMMAB4 model predictions (light blue lines) are also shown. Note that lava data were not used in the derivation of the GGFMB model.

4.2. Dipole Field and Global Paleosecular Variation

First, we use GGFMB to investigate the evolution of the global field (Figure 4) in terms of dipole coefficients, dipole moment (DM), geomagnetic pole latitude (GPL), and globally averaged paleosecular variation index P_i (Panovska & Constable, 2017). The latter can be used to distinguish between stable field state ($P_i < 0.5$) and unstable field state ($P_i \geq 0.5$).

We include the DM, GPL, and P_i parameters calculated from previous models (IMMAB4 and IT08) for comparison. For IT08, we transformed the Gauss coefficients originally provided as relative time steps to an absolute time scale. We assumed that the change in the sign of the axial dipole component occurred at 780 ka and applied a linear interpolation for ages older and younger than 780 ka. This results in an age range of 801–769 ka for the IT08 model. Global stacks of VDM, VGP, and P_i calculated by Mahgoub et al. (2023) from the same input data records as used for the GGFMB inversion are also included in Figure 4.

Most of the time the axial dipole component, g_1^0, is clearly stronger than the equatorial dipole components, h_1^1 and g_1^1 (Figure 4a). These in general varied between plus and minus 10 μT. The axial dipole starts to decline, with continuing fluctuations, around 820 ka. Between ~790–775 ka, the three dipole terms are of comparable magnitudes. Interestingly, the equatorial dipole contributions seem to have lower amplitude variations in this interval and up to ~750 ka. g_1^0 briefly fluctuated at values close to zero at ~775 ka, and then started to recover rapidly and nearly linearly in the normal field direction (negative g_1^0), completing the full global polarity reversal. During this time, the axial dipole was stronger (g_1^0 average = ~−26 μT) than in the late Matuyama (g_1^0 average = ~18 μT), and this trend continued nearly until the end of the studied period.

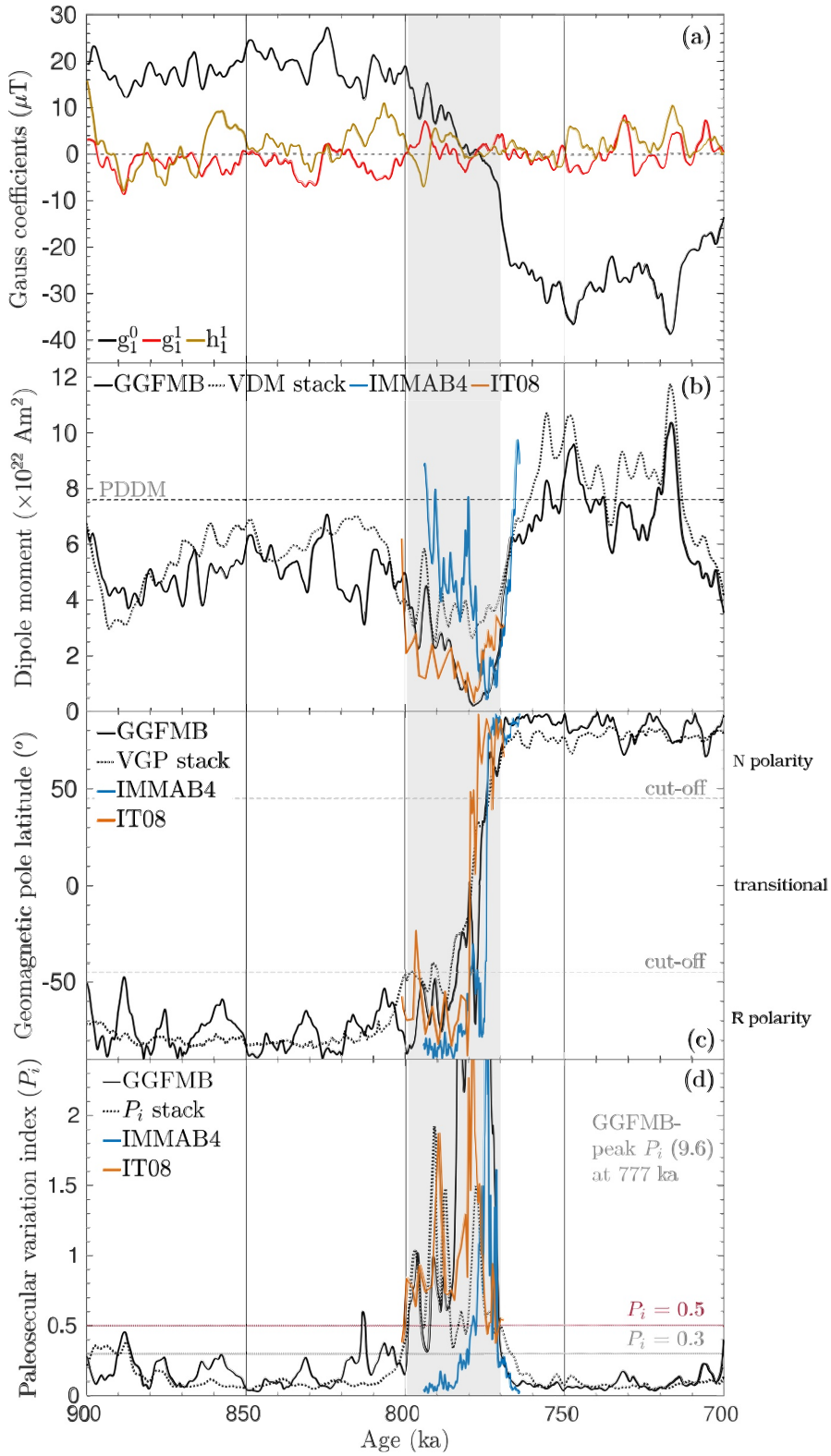

Figure 4. Temporal evolution of: (a) dipole coefficients (colored lines), (b) dipole moment (DM), (c) geomagnetic pole latitude (GPL), and (d) paleosecular variation index (P_i) of the magnetic field during 900–700 ka, estimated from GGFMB model (black lines). The DM, GPL, and P_i curves of models IMMAB4 (Leonhardt & Fabian, 2007) and IT08 (Ingham & Turner, 2008) are included as blue and orange lines, respectively. Stacks of virtual dipole moment (VDM), virtual geomagnetic pole (VGP), and P_i constructed by Mahgoub et al. (2023) are also plotted as dotted black line. The gray box indicates the period 799–770 ka, over which the MB reversal evolved.

The DM (Figure 4b) (calculated from all three dipole component coefficients) largely reflects the dominating axial dipole influence. It decayed from 788 ka until reaching its lowest value (0.1×10^{22} Am^2) at ~780 ka. The DM, then, increased slightly to 0.7×10^{22} Am^2 at 774 ka, before a rapid, nearly linear increase to 6.5×10^{22} Am^2 at 767 ka. This overall evolution clearly demonstrates the asymmetric sawtooth pattern (Meynadier et al., 1994; Valet & Meynadier, 1993) of slow dipole decay and fast recovery described by Ziegler et al. (2011) and Avery et al. (2017). The average DM for the late Matuyama, from 900 to 800 ka, is 5.0×10^{22} Am^2, which is ~65% of the present-day dipole moment (PDDM) = 7.6×10^{22} Am^2, estimated from latest version of International Geomagnetic Reference Field (IGRF), Alken et al. (2021). For the early Brunhes, from 767 to 700 ka, the average DM is 6.9×10^{22} Am^2, almost 90% of the PDDM. The dipole decay starts significantly later in the IMMAB4 model, and the time of minimum DM is offset by ~8 Kyr. The DM of IT08 is relatively similar to our new result. The VDM stack obtained directly from the data records generally has very similar variations to the GGFMB DM, but often slightly higher values, and clearly higher values during the reversal from ~790–770. This bias likely is caused by leakage of non-dipole power from the individual records into the averaged VDM.

GGFMB suggests that the tilt of the dipole field, the geomagnetic pole latitude (GPL), Figure 4c, varied notably during the late Matuyama. It reached values of −48° and −50° at 888 ka and 807 ka, respectively, and of around −60° four more times. GPL between +45° and −45° may be considered as transitional polarity state. The full polarity transition started at 784 ka and ended at 773 ka, when the magnetic field entered the Brunhes normal polarity state. Prior to 784 ka, low GPL values (~−50°) were seen at 794 ka and 791 ka. After the polarity transition, the dipole tilt variations were less pronounced than during the late Matuyama. The GPL curves of the IMMAB4 and IT08 models differ slightly and indicate that polarity transition occurred over the time period ~780–773 ka. The VGP stack (Mahgoub et al., 2023) agrees quite well with the GGFMB GPL, but with less variability in the late Matuyama.

The paleosecular variation index P_i (Figure 4d) mostly lies clearly below the threshold of 0.5 during the late Matuyama, but reaches or slightly exceeds it around 888 ka and 813 ka. Moreover, several peaks occur in the P_i curve from ~800 ka before the strong peak that marks the main polarity transition at ~777 ka (Figure 4d). According to the globally averaged P_i of GGFMB model, the MB reversal evolved between 799 and 770 ka, with the main, global polarity swing occurring between ~792 and 770 ka. A small peak in P_i can be observed at 796 ka, which correlates to the MB precursor event observed at 795 ka by Hartl and Tauxe (1996). Two additional small peaks were detected at 791 ka and 788 ka, which can be considered as two precursor events. A transitional state, associated with a small peak in P_i, can be also noted around 813 ka, which may have been an earlier precursor event, or it may represent a distinct excursion, that happened prior to the MB reversal. The P_i peak around 888 ka is related to the Kamikatsura excursion, as will be discussed further in Section 4.5. There are three additional periods(~876, 857, and 831 ka) with rather high P_i values ~0.3 (Figure 4d), noted in distinct regions rather than globally (See Movie S1), which are compatible with the suggestion that three regional excursions took place in the late Matuyama. Younger excursions, such as the Mono Lake/Auckland (around 31 ka) and the Norwegian-Greenland Sea (around 65 ka), have comparable P_i values (See Panovska et al., 2021). No transitional field state is found in the early Brunhes, between 770 and 700 ka. Comparing the P_i curves from the earlier models (Figure 4d), IT08 gives rather similar results to GGFMB, while IMMAB4 suggests a much shorter duration of the reversal, from 779 ka to 771 ka. The global P_i stack, on the other hand, gives a similar duration as GGFMB, from 799 to 770 ka, but with different peaks in the early phase of the reversal.

4.3. Non-Dipole Power Evolution

The distribution of dipole power (DP) and non-dipole power (NDP) may provide constraints on the processes in Earth's core during the reversal. First, we consider the geomagnetic power spectra of GGFMB to assess the model resolution. Figure 5 shows spatial power spectra up to SH degree 6 of the time-averaged field (TAF) of GGFMB and its secular variation in comparison to the time-averaged GUFM historical model (1590–1990; Jackson et al., 2000) and the IGRF for 2005 (Alken et al., 2021). The averaged GGFMB main field has comparable power to the present-day and historical field up to about SH degree 4. The drop in power in degrees 5 and 6 indicates a lack of resolution for spatial scales smaller than SH degree 4 in GGFMB. The model also clearly has less power in secular variation at all spatial scales, indicating that the temporal resolution of GGFMB is notably lower than geomagnetic field variations seen in the present-day field.

The evolution of DP and NDP at the core-mantle boundary (CMB) and at the Earth's surface is displayed in Figure 6. The NDP is limited by the spatial model resolution, and NDP in the following always refers to large-scale NDP up to SH degree around 5. Both in the late Matuyama and the early Brunhes, the NDP at the CMB varies at

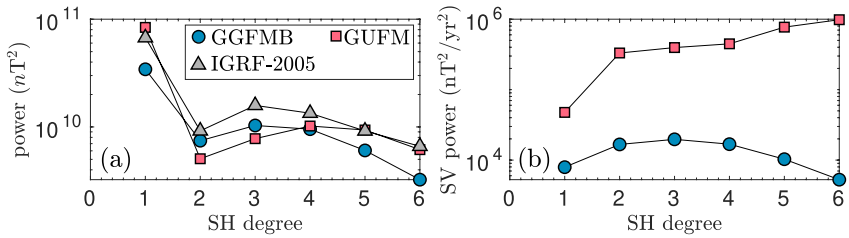

Figure 5. Comparison of geomagnetic power spectra of main field (left) and secular variation (right) of our GGFMB model with the GUFM (Jackson et al., 2000) and IGRF 2005 (Alken et al., 2021) models, both at the core-mantle boundary.

a level on average slightly lower than the DP, but occasionally reaching or surpassing it. At Earth's surface the DP clearly dominates at these times. GGFMB suggests that the NDP rises above the late Matuyama average in the early phase of the MB reversal (ca. 800–782 ka), and then drops slightly during the minimum in DP. The previous prediction by IMMAB4 is somewhat similar, though the average NDP increase starts later there (~783 ka) and drops further after a short increase that coincides with the DP increase.

4.4. The MB Reversal

We now take a closer look at the evolution of the MB reversal. Figure 7 shows snapshots of surface field intensity (F), P_i, and radial field (B_r) at the CMB. Movie S1 provides a continuous display of these parameters along with others, including magnetic field inclination, the DP, and the NDP. The first three snapshots in the figure (Figure 7a–7c) cover the Kamikatsura excursion, which will be discussed in Section 4.5.

In the late Matuyama (Figure 7d) the field was comparatively high at 825 ka, reaching ~70 μT in some high-latitude northern hemisphere regions. At 813 ka (Figure 7e), low field strength associated with a strong reverse flux patch is seen in the high latitude North Pacific area (150°–150°W), and P_i exceeds 0.5 there and at high southern latitudes. We note that one reverse flux patch, between North America and Siberia, crosses the tangent cylinders (TC) at this time. This anomalous field behavior is maintained for ~1 Kyr (until 812 ka). As was previously indicated, this period is regarded as either a precursor to the MB reversal or a distinct excursion during Late-Matuyama. It is clear from the P_i map that the anomalous field state at 813 ka is regional rather than global. At the CMB, the DP decreased slightly and the NDP clearly increased during this time (Figure 6). After 812 ka, the magnetic field returned to its previous stable Late-Matuyama dipole state. This continues up until 799 ka (Figure 7f), at which point the DM (Figure 4) began to steadily drop, and this is the time when MB reversal started. At this time (799 ka), the field strength became weak in several parts of the world. This decrease in field strength is related to the growth of two reverse flux patches under Siberia and North America, and a reverse flux patch under the Indian Ocean in the southern hemisphere that reaches into the TC. At Earth's surface, the global P_i map indicates that regions of Antarctica, Australia, and the Indian Ocean first witnessed of the starting of the reversal. The mid-point of the reversal occurred 780 Kyr ago (Figure 7g), where most of the world was in a transitional field state. At this time, the DM was near to zero, and the NDP was low at Earth's surface. After 780 ka, the magnetic field slowly started to configure into the new Brunhes normal polarity (Figure 7h). From 770 ka on, the DM, ADM, DP, and NDP started to rise quickly, recovering to a stable field configuration that marks the end of the MB reversal. Transitional field states were last found in the regions of North America, Southern Africa, Indian Ocean, and southern Australia.

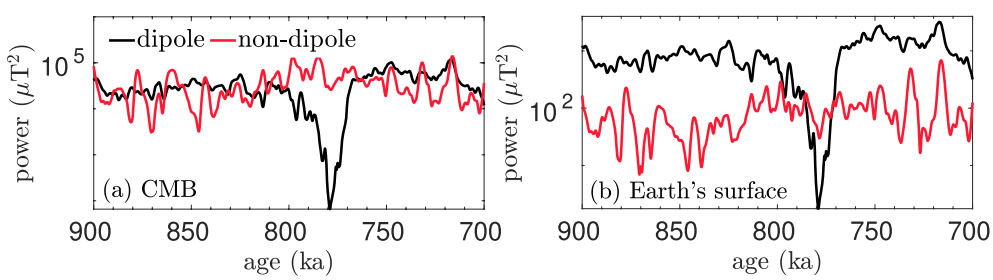

Figure 6. 900–700 ka evolution of the dipole and non-dipole power (a) the CMB and (b) at the Earth's surface, calculated from the GGFMB model.

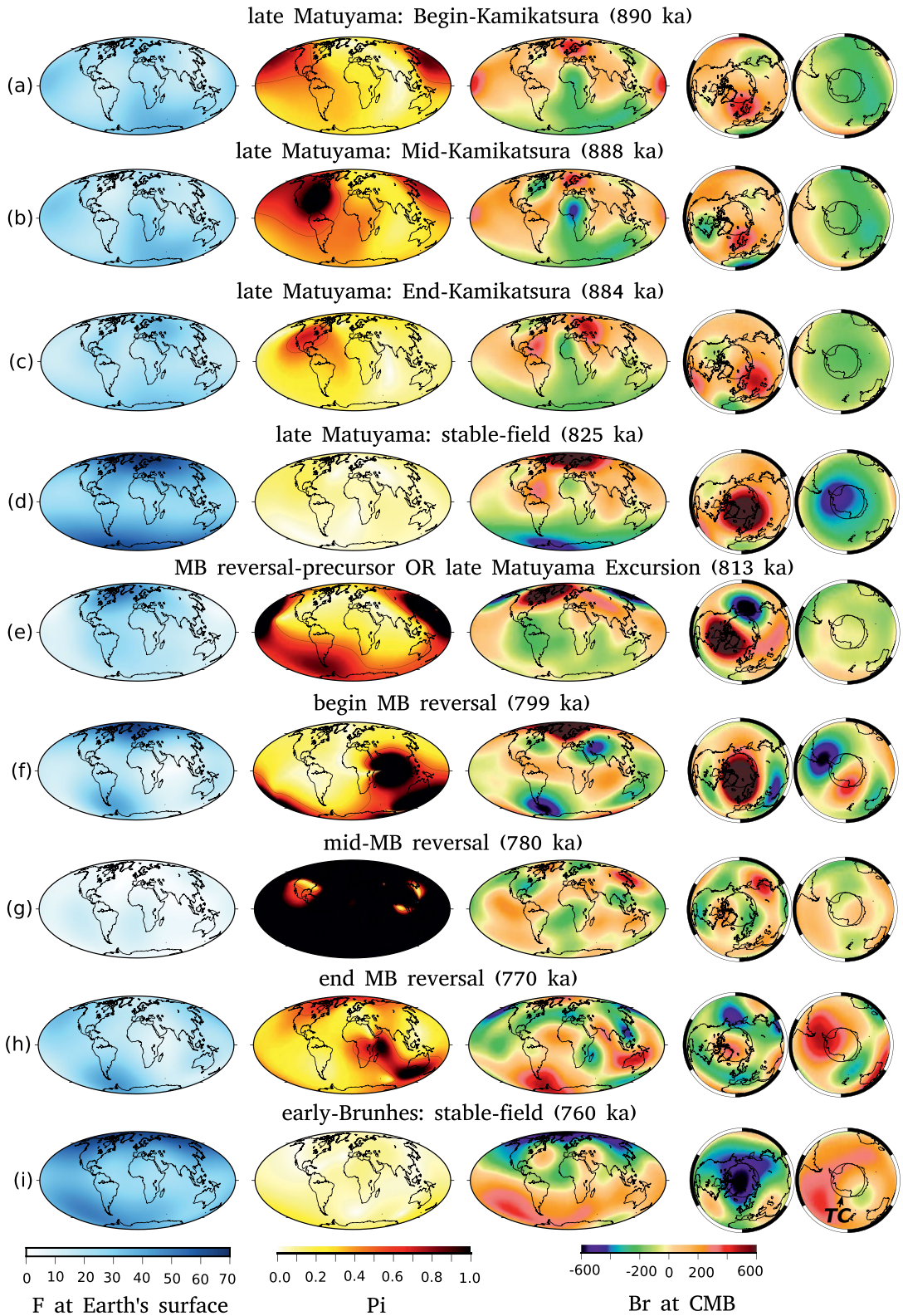

Figure 7. Snapshots show field morphology of the magnetic field between 900 and 700 ka, according to GGFMB model, in terms of (left to right) magnetic field intensity (F) at Earth's surface; Paleosecular variation index (P_i); and radial field component (B_r) at core-mantle boundary (CMB). F and B_r are expressed in μT, whereas P_i is dimensionless. Blue and red shades in B_r maps indicate outward and inward-directed radial field, respectively.

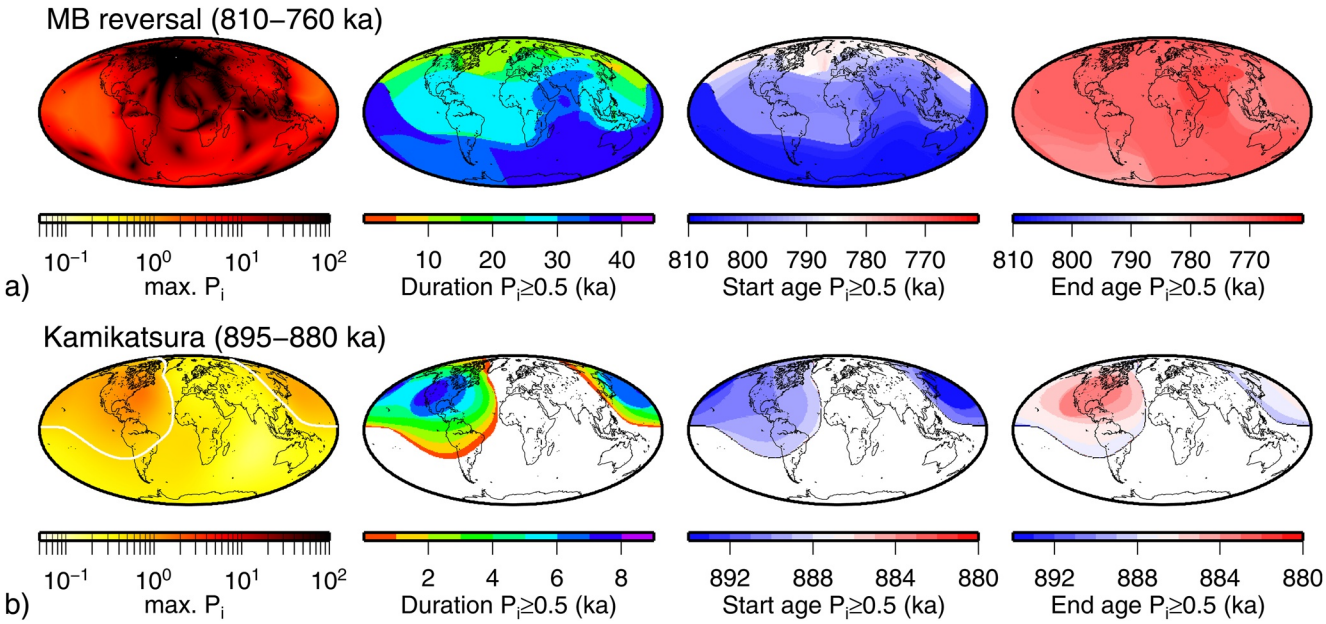

Figure 8. Two panels display (from left to right) the maximum P_i, regional duration, the starting age, and the ending age of MB reversal (a) and Kamikatsura excursion (b), estimated using a P_i threshold value of 0.5 (Panovska & Constable, 2017). Note that white areas on maps of the Kamikatsura excursion represent $P_i < 0.5$.

The last line of snapshots (Figure 7i) shows the field morphology at 760 ka as example of the new polarity in the Brunhes chron.

Figure 8a displays maps of maximum P*i* calculated over the period 810–760 ka, and of the length, start age, and end age of the MB reversal, calculated using a P_i threshold value of 0.5. The P*i* reached regionally different maximum values at different times during MB. The highest values occurred in the mid- to high-latitude regions of the North Atlantic. The duration ranges regionally from ∼10 to ∼30 Kyr. GGFMB suggests that in general the duration increases from the northern to the southern hemisphere, and that the reversal evolved starting from the southern hemisphere. Exceptions from this trend can be seen in the region around the Indian Ocean and at longitudes around 180°E, where a large duration (∼30 Kyr) was observed also at equatorial latitudes. Unlike the lateral variation of duration and start age, the end of MB reversal was seen nearly concurrently around the globe.

4.5. The Kamikatsura Excursion (∼890–884 ka)

The Kamikatsura excursion is named after the Japanese mountain range's Kamikatsura Tuff (Maenaka, 1983). Different authors proposed the occurrence of this excursion using various rock types, such as sediment cores (Channell & Kleiven, 2000; Xuan et al., 2016), lavas (Camps et al., 2011; Coe et al., 2004; Singer et al., 1999), and loess deposits (Wang et al., 2010; Yang et al., 2004). As for the MB, there is an ongoing debate concerning the age of the Kamikatsura excursion (for more details, see Laj & Channell, 2015; Channell et al., 2020). An initial age of 890 ka was determined from tuff sediments (Maenaka, 1983). This age is comparable to the age of 888 ka, which was determined from IODP Site U1304 (Xuan et al., 2016). However, these ages differ from the age of 868 ka, obtained from IODP Site U1305 (Channell, 2017; Mazaud et al., 2012), according to oxygen isotope data of Hillaire-Marcel et al. (2011). Channell et al. (2020) estimated a weighted mean age of 867 ± 2 ka, using $^{40}Ar/^{39}Ar$ age data (recalibrated to Fish Canyon sanidine standard age of 28.201 Ma; Kuiper et al., 2008) of three Hawaiian lava flows (Coe et al., 2004; Singer et al., 2019) and one lava from Tahiti (Chauvin et al., 1990; Singer et al., 1999, 2019).

The GGFMB P_i curve (Figure 4d) indicates an excursion at 890–884 ka, which is related to Kamikatsura excursion (Maenaka, 1983). This age is consistent with the age of 888 ka for the Kamikatsura excursion calculated from Tuffs (Maenaka, 1983) and sediment records (Xuan et al., 2016), so we consider it to be this event. However, note that the age disagrees with the age determined by Channell et al. (2020) from lavas (867 ka). During the Kamikatsura, the NDP increased and reached values greater than the DP at the CMB (Figure 6). The DM and

the ADM decreased to ~4.0 × 10^{22} Am^2 and ~3.0 × 10^{22} Am^2, respectively. These values are comparable to other excursions, for example, the Mono Lake excursion, encountered during the past 100 ka (See Panovska et al., 2021).

Figures S5 and S52 in Supporting Information S1 describe and illustrate the paleomagnetic data (VDM, VGP, and P*i*) reported from lavas and sediment records of the age range 900–860ka. GGFMB DM, GPL, and P*i* estimates are also shown in more detail than in Figure 4 together with VDM and VGP results from the individual records. We note that North Atlantic records had transitional polarity state at 892–890 ka, 890–884 ka, and 880–870 ka. Notably, at 890–884 ka, the VDM of these records was less than 4 × 10^{22} Am^2, the VGP latitude >−45°, and $P_i \geq 0.5$. This likely represents the Kamikatsura excursion. No transitional directions were seen in lava sites throughout this interval, while transitional directions were observed at 880–863 ka (See Figure S52 in Supporting Information S1). Taking into account the large age uncertainty of the lavas, it is possible that these transitional directions also belong to the Kamikatsura excursion.

Snapshots of F, P_i, and Br, are shown for three times around the Kamikatsura excursion in Figure 7. GGFMB indicates that the excursion started at ~890 ka with weak field intensity, associated with two reverse flux patches that appeared under the eastern North America and eastern Siberia. A large area of high P_i activity was seen in these regions during this time. At Earth's surface, the P_i maps show that the Kamikatsura excursion was seen in North America and eastern Asia, which is also confirmed by the maximum P_i map (Figure 8). The magnetic field weakened between 890 and 886 ka, with the North American reverse flux patch growing and the Siberian reverse flux contracting (Movie S1). The excursion reached its maximum extension at 888 ka (Figures 7 and 8), and its duration regionally varied from ~1–6 Kyr (Figure 8). Around 884 ka, when the North American reverse flux patch moved north and largely disappeared, the excursion came to an end (Figures 7 and 8).

4.6. Time-Averaged Field

We investigate the average field configuration before, during, and after the MB reversal by looking at the time-averaged field (TAF) for the late Matuyama (900–799 ka), the MB reversal (799–770 ka) and the early Brunhes (770–700 ka) intervals. The TAF components of surface field intensity (F), radial field (B_r) at the CMB, and the non-axial dipole (NAD) field of the B_r (eliminating g_1^0) at the CMB are given in Figure 9. The TAF is clearly dipole dominated in the Late Matuyama (Figure 9a) and early Brunhes (Figure 9c) intervals, with higher intensities in the latter interval, consistent with the higher dipole moment after than before the reversal (Figure 4b). The B_r map over late Matuyama shows two high latitude flux lobes surrounding the TC in the Northern Hemisphere, over eastern North America and eastern-central Asia. These two flux lobes are not visible in the early Brunhes. Instead, the average NAD structure is similar before and after the reversal, creating the clear intense flux patches in B_r when the dipole flux is in the same direction as the NAD patches, but weakening the field in these regions when the dipole polarity is opposite. We find less field structure in the southern hemisphere, which might reflect the nonhomogeneous distribution of the input data with less data originating from the southern hemisphere (Figure 1a).

During the reversal (Figure 9b), the average intensity did not exceed 20 μT, and the lowest values (≤5 μT) are found in the regions Antarctica-Australia, northeast Africa-west Asia, and Mesoamerica. B_r and its NAD contribution are very similar as the axial dipole was near zero. The average field configuration at this time is surprisingly comparable to the NAD averages before and after, however, with reverse sign in the two northern intense flux patches. Note that the NAD flux in GGFMB is highly variable and individual epoch snapshots often do not resemble these averages (See Movie S1). We also note that the GGFMB TAF during the reversal differs clearly from the averages given by the earlier models IMMAB4 and IT08 (see Figure S51 in Supporting Information S1). These also clearly differ from each other, both in terms of average radial field configuration and regions of lowest intensities.

We calculated the TAF for two more models, GGF100k (Panovska et al., 2018) and CALS10k.2 (Constable et al., 2016), to investigate whether the average magnetic field during late Matuyama and early Brunhes resembles the more recent times. GGF100k covers the past 100 ka, whereas CALS10K.2 covers the past 10 ka. To be consistent with our GGFMB model, the TAF is computed up to SH degree 6 and the time-averaged F, B_r, and NAD of B_r are plotted (Figures 9d and 9e). The high average field intensity, which reached 70–75 μT, and the prominence of the axial dipole moment in GGF100k and CALS10k are comparable to the early Brunhes but

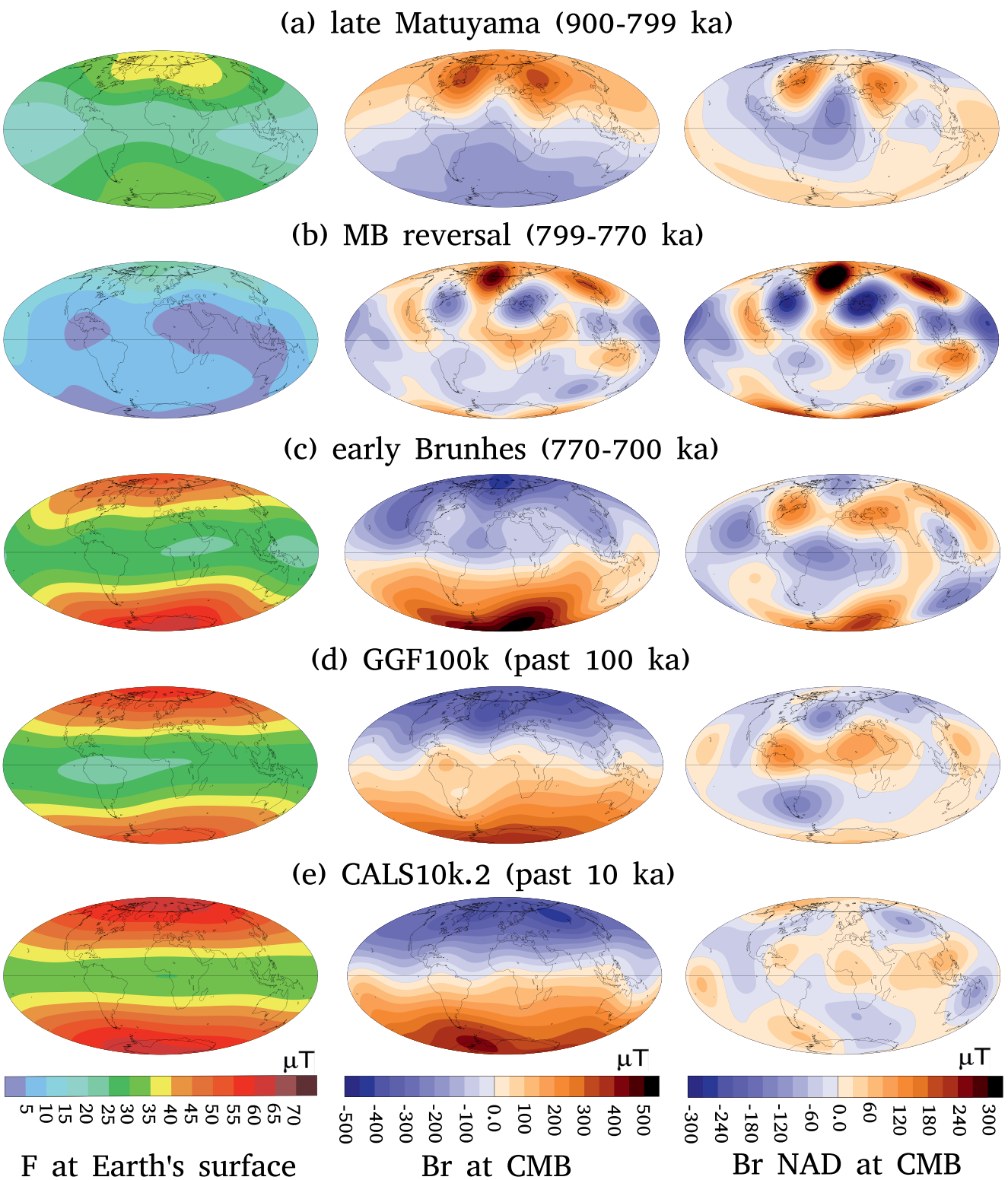

Figure 9. Time-averaged field (TAF) of field intensity (F) at the Earth's surface (left), radial field (B_r) at the CMB (middle), and non-axial dipole (NAD) part of B_r at the CMB (right) for different time intervals: late Matuyama (a), MB reversal (b) and early Brunhes (c) from GGFMB, and compared to the 100 Kyr average of model GGF100k (d; Panovska et al., 2018) and the 10 Kyr average of model CALS10k.2 (e; Constable et al., 2016). Note that maps of B_r and NAD of B_r are on different scales.

higher than the late Matuyama. The B_r in CALS10k.2 has two patches of intense normal flux in the Northern Hemisphere, which is comparable to those observed in late Matuyama. The averaged B_r NAD field of GGF100k and CALS10k.2 exhibit distinguishing characteristics from late Matuyama and early Brunches. For example, GGF100k and CALS10k.2 have two areas of positive flux between Mesoamerica and Central Africa, whereas the late Matuyama and early Brunhes had negative flux in these regions. Intense flux patches in the northern hemisphere appear at different longitudes in the various averages. An area of positive NAD flux over western Antarctica is found in all models, while the average field in the eastern southern high latitudes vary substantially. If the late Matuyama represented the typical field behavior preceding a reversal, this might suggest that the next reversal is not imminent, which is consistent with previous suggestion based on field morphology (Brown et al., 2018; Constable & Korte, 2006).

5. Conclusions

The Matuyama-Brunhes (MB) reversal, late Matuyama, and early Brunhes periods are examined using a newly derived global geomagnetic field model for the (Matuyama-Brunhes reversal), GGFMB. Thirty-eight high-quality sediment records spanning the period from 900 to 700 ka with independent age control, which were selected and compiled by Mahgoub et al. (2023), were used as input data for this model. These records have a reasonable global distribution, and their quantity is clearly higher than for earlier MB reversal models. Nevertheless, the western and southern hemispheres are still underrepresented in the available data. GGFMB is constructed up to spherical harmonic degree 6, but power spectra analysis shows that its effective spatial resolution is up to about degree 4. The model properly predicts the majority of the independent TRM data acquired from well-dated lavas, lending credibility to it. Our reconstruction shows that, aside from the MB reversal period when axial dipole (g_1^0) and equatorial dipole components (g_1^1 and h_1^1) were of the same magnitude, the period 900–700 ka was dominated by the axial dipole field component. The dipole moment during the late Matuyama was low compared to the Early-Brunhes and the recent past 100 Kyrs.

The GGFMB paleosecular variation index indicates that the MB reversal globally took place over a 29 Kyr period between 799 and 770 ka, while in some regions it manifested itself over no more than 10 Kyr. The magnetic field was in a transitional state (low geomagnetic pole latitude and dipole moment), ~10 Kyr earlier (at 813 ka), which is either a precursor of the MB reversal or a separate excursion. At this time, a strong reverse flux patch is seen between 150°E and 150° W at northern high latitudes. In contrast to NDP, which clearly increased, there was only a small drop in the DP. At 799 ka, when the reversal started, anomalous field behavior started to appear in the high-latitude southern hemisphere and equatorial regions. This was accompanied by two reverse flux patches appearing beneath Siberia and North America. At this time, the NDP increased while the DP began to decrease. Nearly the entire planet entered a transitional field state at 780 ka, when the DP collapsed and the NDP also dropped slightly, and the axial dipole reached zero. The DP, subsequently, started to increase in the opposite direction, and recovered in strength to complete the global polarity reversal. The magnetic field took ~10 Kyr, after 780 ka, to enter the stable early Brunhes chron. The observed dipole behavior agrees with the sawtooth pattern of slower decay than recovery reported from the past 2 Myr in general and reversals in particular.

Beside the reversal, GGFMB shows a regional excursion at 890–884 ka, which is considered to be the Kamikatsura excursion. The axial dipole shows a small drop in strength, and also the equatorial dipole terms and most of the non-dipole terms decreased. Two weak reverse flux patches, below eastern North America and eastern Siberia, generated this excursion, which lasted for a ~6 Kyr according to the globally averaged P_i. According to GGFMB, Kamikatsura is observed along North and Eastern America and Eastern Asia. Three further possible regional excursions are noted at 876 ka, 857 ka, and 831 ka in the late Matuyama, when the dipole moment generally was lower than in the early Brunhes and the past 100 Kyr. The first two seem to be caused more by increase of NDP rather than decrease of DP. However, to confirm and fully comprehend all of these excursions, further high-resolution sediment records are required. Moreover, we have not considered effects of pDRM smoothing, lock-in delays or age uncertainties in general. A study to better constrain the robustness of features found in GGFMB is already in process, that will partly address these issues.

Data Availability Statement

The manuscript includes a Supporting Information S1 file with all of the supplementary sections and figures. The model Gauss coefficients, dipole moment, and Paleosecular variation index can be found at https://earthref.org/ERDA/2548/. An animation of the GGFMB model (Movie S1) is available at https://earthref.org/ERDA/2549/.

Acknowledgments
The Alexander von Humboldt Foundation awarded A.N. Mahgoub a research fellowship, which he expressed thanks for. S. Panovska gratefully acknowledges the Discovery Fellowship at the GFZ Potsdam, Germany. We appreciate the helpful comments and suggestions from Gillian Turner and an anonymous reviewer, which improved aspects of the paper. We would like to express a deep appreciation to all authors who shared their data with us personally, or made the data available through Supporting Information S1 and public databases. Open access funding enabled and organized by Projekt DEAL.

References

Alken, P., Thébault, E., Beggan, C. D., Amit, H., Aubert, J., Baerenzung, J., et al. (2021). International geomagnetic reference field: The thirteenth generation. *Earth Planets and Space*, *73*(1), 1–25. https://doi.org/10.1186/s40623-020-01288-x

Amit, H., Leonhardt, R., & Wicht, J. (2010). Polarity reversals from paleomagnetic observations and numerical dynamo simulations. *Space Science Reviews*, *155*(1), 293–335. https://doi.org/10.1007/s11214-010-9695-2

Arason, P., & Levi, S. (1990). Compaction and inclination shallowing in deep-sea sediments from the Pacific Ocean. *Journal of Geophysical Research*, *95*(B4), 4501–4510. https://doi.org/10.1029/jb095ib04p04501

Aubert, J., Finlay, C. C., & Fournier, A. (2013). Bottom-up control of geomagnetic secular variation by the Earth's inner core. *Nature*, *502*(7470), 219–223. https://doi.org/10.1038/nature12574

Avery, M. S., Gee, J. S., & Constable, C. G. (2017). Asymmetry in growth and decay of the geomagnetic dipole revealed in seafloor magnetization. *Earth and Planetary Science Letters*, *467*, 79–88. https://doi.org/10.1016/j.epsl.2017.03.020

Backus, G., George, B., Parker, R. L., Parker, R., & Constable, C. (1996). *Foundations of geomagnetism*. Cambridge University Press.

Benton, E. R., & Whaler, K. A. (1983). Rapid diffusion of the poloidal geomagnetic field through the weakly conducting mantle: A perturbation solution. *Geophysical Journal International*, *75*(1), 77–100. https://doi.org/10.1111/j.1365-246x.1983.tb01914.x

Bieber, A., St-Onge, G., Feuillet, N., Carlut, J., Moreno, E., & Michel, E. (2021). Regional chronostratigraphy in the eastern Lesser Antilles quaternary fore-arc and accretionary wedge sediments: Relative paleointensity, oxygen isotopes and reversals. *Quaternary Geochronology*, *65*, 101179. https://doi.org/10.1016/j.quageo.2021.101179

Bloxham, J., & Jackson, A. (1992). Time-dependent mapping of the magnetic field at the core-mantle boundary. *Journal of Geophysical Research*, *97*(B13), 19537–19563. https://doi.org/10.1029/92jb01591

Brown, M. C., Korte, M., Holme, R., Wardinski, I., & Gunnarson, S. (2018). Earth's magnetic field is probably not reversing. *Proceedings of the National Academy of Sciences*, *115*(20), 5111–5116. https://doi.org/10.1073/pnas.1722110115

Camps, P., Singer, B., Carvallo, C., Goguitchaichvili, A., Fanjat, G., & Allen, B. (2011). The Kamikatsura event and the Matuyama–Brunhes reversal recorded in lavas from Tjörnes Peninsula, northern Iceland. *Earth and Planetary Science Letters*, *310*(1–2), 33–44. https://doi.org/10.1016/j.epsl.2011.07.026

Channell, J. E. T. (2017). Complexity in Matuyama–Brunhes polarity transitions from North Atlantic IODP/ODP deep-sea sites. *Earth and Planetary Science Letters*, *467*, 43–56. https://doi.org/10.1016/j.epsl.2017.03.019

Channell, J. E. T., Curtis, J. H., & Flower, B. P. (2004). The Matuyama-Brunhes boundary interval (500-900 ka) in North Atlantic drift sediments. *Geophysical Journal International*, *158*(2), 489–505. https://doi.org/10.1111/j.1365-246x.2004.02329.x

Channell, J. E. T., Hodell, D. A., Singer, B. S., & Xuan, C. (2010). Reconciling astrochronological and $^{40}Ar/^{39}Ar$ ages for the Matuyama-Brunhes boundary and late Matuyama Chron. *Geochemistry, Geophysics, Geosystems*, *11*(12), Q0AA12. https://doi.org/10.1029/2010gc003203

Channell, J. E. T., Hodell, D. A., Xuan, C., Mazaud, A., & Stoner, J. S. (2008). Age calibrated relative paleointensity for the last 1.5 Myr at IODP Site U1308 (North Atlantic). *Earth and Planetary Science Letters*, *274*(1–2), 59–71. https://doi.org/10.1016/j.epsl.2008.07.005

Channell, J. E. T., & Kleiven, H. F. (2000). Geomagnetic palaeointensities and astrochronological ages for the Matuyama–Brunhes boundary and the boundaries of the Jaramillo Subchron: Palaeomagnetic and oxygen isotope records from ODP site 983. *Philosophical Transactions of the Royal Society of London,Series A: Mathematical, Physical and Engineering Sciences*, *358*(1768), 1027–1047. https://doi.org/10.1098/rsta.2000.0572

Channell, J. E. T., McManusLehman, D. A. J. B., McManus, J., & Lehman, B. (1998). Orbital modulation of the Earth's magnetic field intensity. *Nature*, *394*(6692), 464–468. https://doi.org/10.1038/28833

Channell, J. E. T., & Raymo, M. E. (2003). Paleomagnetic record at ODP site 980 (Feni drift, Rockall) for the past 1.2 Myrs. *Geochemistry, Geophysics, Geosystems*, *4*(4). https://doi.org/10.1029/2002gc000440

Channell, J. E. T., Singer, B. S., & Jicha, B. R. (2020). Timing of Quaternary geomagnetic reversals and excursions in volcanic and sedimentary archives. *Quaternary Science Reviews*, *228*, 106114. https://doi.org/10.1016/j.quascirev.2019.106114

Channell, J. E. T., Wright, J. D., Mazaud, A., & Stoner, J. S. (2014). Age through tandem correlation of Quaternary relative paleointensity (RPI) and oxygen isotope data at IODP Site U1306 (Eirik Drift, SW Greenland). *Quaternary Science Reviews*, *88*, 135–146. https://doi.org/10.1016/j.quascirev.2014.01.022

Chauvin, A., Roperch, P., & Duncan, R. A. (1990). Records of geomagnetic reversals from volcanic islands of French Polynesia: 2. Paleomagnetic study of a flow sequence (1.2–0.6 Ma) from the island of Tahiti and discussion of reversal models. *Journal of Geophysical Research*, *95*(B3), 2727–2752. https://doi.org/10.1029/jb095ib03p02727

Clement, B. M. (2004). Dependence of the duration of geomagnetic polarity reversals on site latitude. *Nature*, *428*(6983), 637–640. https://doi.org/10.1038/nature02459

Coe, R. S., Singer, B. S., Pringle, M. S., & Zhao, X. (2004). Matuyama–Brunhes reversal and Kamikatsura event on Maui: Paleomagnetic directions, $^{40}Ar/^{39}Ar$ ages and implications. *Earth and Planetary Science Letters*, *222*(2), 667–684. https://doi.org/10.1016/j.epsl.2004.03.003

Constable, C., & Korte, M. (2006). Is Earth's magnetic field reversing? *Earth and Planetary Science Letters*, *246*(1–2), 1–16. https://doi.org/10.1016/j.epsl.2006.03.038

Constable, C., Korte, M., & Panovska, S. (2016). Persistent high paleosecular variation activity in southern hemisphere for at least 10 000 years. *Earth and Planetary Science Letters*, *453*, 78–86. https://doi.org/10.1016/j.epsl.2016.08.015

Dagley, P., & Lawley, E. (1974). Palaeomagnetic evidence for the transitional behaviour of the geomagnetic field. *Geophysical Journal International*, *36*(3), 577–598. https://doi.org/10.1111/j.1365-246x.1974.tb00614.x

Deamer, G. A., & Kodama, K. P. (1990). Compaction-induced inclination shallowing in synthetic and natural clay-rich sediments. *Journal of Geophysical Research*, *95*(B4), 4511–4529. https://doi.org/10.1029/jb095ib04p04511

De Boor, C. (2001). *A practical guide to splines* (Revised Edition). Springer-Verlag.

Dinarès-Turell, J., Sagnotti, L., & Roberts, A. P. (2002). Relative geomagnetic paleointensity from the Jaramillo Subchron to the Matuyama/Brunhes boundary as recorded in a Mediterranean piston core. *Earth and Planetary Science Letters*, *194*(3–4), 327–341. https://doi.org/10.1016/s0012-821x(01)00563-5

Fisher, R. A. (1953). Dispersion on a sphere. *Proceedings of the Royal Society of London. Series A. Mathematical and Physical Sciences*, *217*(1130), 295–305. https://doi.org/10.1098/rspa.1953.0064

Glatzmaiers, G. A., & Roberts, P. H. (1995). A three-dimensional self-consistent computer simulation of a geomagnetic field reversal. *Nature*, *377*(6546), 203–209. https://doi.org/10.1038/377203a0

Gubbins, D. (1975). Can the Earth's magnetic field be sustained by core oscillations? *Geophysical Research Letters*, *2*(9), 409–412. https://doi.org/10.1029/gl002i009p00409

Gubbins, D. (1983). Geomagnetic field analysis—I. Stochastic inversion. *Geophysical Journal International*, *73*(3), 641–652. https://doi.org/10.1111/j.1365-246x.1983.tb03336.x

Guyodo, Y., Acton, G. D., Brachfeld, S., & Channell, J. E. (2001). A sedimentary paleomagnetic record of the Matuyama chron from the Western Antarctic margin (ODP Site 1101). *Earth and Planetary Science Letters*, *191*(1–2), 61–74. https://doi.org/10.1016/s0012-821x(01)00402-2

Guyodo, Y., & Valet, J.-P. (1999). Global changes in intensity of the Earth's magnetic field during the past 800 Kyr. *Nature*, *399*(6733), 249–252. https://doi.org/10.1038/20420

Haneda, Y., Okada, M., Suganuma, Y., & Kitamura, T. (2020). A full sequence of the Matuyama–Brunhes geomagnetic reversal in the Chiba composite section, Central Japan. *Progress in Earth and Planetary Science*, *7*(1), 1–22. https://doi.org/10.1186/s40645-020-00354-y

Hartl, P., & Tauxe, L. (1996). A precursor to the Matuyama/Brunhes transition-field instability as recorded in pelagic sediments. *Earth and Planetary Science Letters*, *138*(1–4), 121–135. https://doi.org/10.1016/0012-821x(95)00231-z

Hayashida, A., Verosub, K. L., Heider, F., & Leonhardt, R. (1999). Magnetostratigraphy and relative palaeointensity of late Neogene sediments at ODP Leg 167 site 1010 off Baja California. *Geophysical Journal International*, *139*(3), 829–840. https://doi.org/10.1046/j.1365-246x.1999.00979.x

Hillaire-Marcel, C., de Vernal, A., & McKay, J. (2011). Foraminifer isotope study of the Pleistocene Labrador Sea, northwest North Atlantic (IODP Sites 1302/03 and 1305), with emphasis on paleoceanographical differences between its "inner" and "outer" basins. *Marine Geology*, *279*(1–4), 188–198. https://doi.org/10.1016/j.margeo.2010.11.001

Horng, C.-S., Lee, M.-Y., Palike, H., Wei, K.-Y., Liang, W.-T., Iizuka, Y., & Torii, M. (2002). Astronomically calibrated ages for geomagnetic reversals within the Matuyama chron. *Earth Planets and Space*, *54*(6), 679–690. https://doi.org/10.1186/bf03351719

Horng, C.-S., Roberts, A. P., & Liang, W.-T. (2003). A 2.14-Myr astronomically tuned record of relative geomagnetic paleointensity from the western Philippine Sea. *Journal of Geophysical Research*, *108*(B1), 2059. https://doi.org/10.1029/2001jb001698

Hyodo, M., Biswas, D. K., Noda, T., Tomioka, N., Mishima, T., Itota, C., & Sato, H. (2006). Millennial-to submillennial-scale features of the Matuyama-Brunhes geomagnetic polarity transition from Osaka Bay, southwestern Japan. *Journal of Geophysical Research*, *111*(B2), B02103. https://doi.org/10.1029/2004jb003584

Hyodo, M., & Kitaba, I. (2015). Timing of the Matuyama–Brunhes geomagnetic reversal: Decoupled thermal maximum and sea-level highstand during marine isotope stage 19. *Quaternary International*, *383*, 136–144. https://doi.org/10.1016/j.quaint.2015.01.052

Ingham, M., & Turner, G. (2008). Behaviour of the geomagnetic field during the Matuyama–Brunhes polarity transition. *Physics of the Earth and Planetary Interiors*, *168*(3–4), 163–178. https://doi.org/10.1016/j.pepi.2008.06.008

Jackson, A., Jonkers, A. R., & Walker, M. R. (2000). Four centuries of geomagnetic secular variation from historical records. *Philosophical Transactions of the Royal Society of London,Series A: Mathematical, Physical and Engineering Sciences*, *358*(1768), 957–990. https://doi.org/10.1098/rsta.2000.0569

Jouzel, J., Masson-Delmotte, V., Cattani, O., Dreyfus, G., Falourd, S., Hoffmann, G., et al. (2007). Orbital and millennial Antarctic climate variability over the past 800,000 years. *Science*, *317*(5839), 793–796. https://doi.org/10.1126/science.1141038

Korff, L., Von Dobeneck, T., Frederichs, T., Kasten, S., Kuhn, G., Gersonde, R., & Diekmann, B. (2016). Cyclic magnetite dissolution in Pleistocene sediments of the abyssal northwest Pacific Ocean: Evidence for glacial oxygen depletion and carbon trapping. *Paleoceanography*, *31*(5), 600–624. https://doi.org/10.1002/2015pa002882

Korte, M., Donadini, F., & Constable, C. (2009). Geomagnetic field for 0–3 ka: 2. A new series of time-varying global models. *Geochemistry, Geophysics, Geosystems*, *10*(6), Q06008. https://doi.org/10.1029/2008gc002297

Kuiper, K., Deino, A., Hilgen, F., Krijgsman, W., Renne, P., & Wijbrans, J. (2008). Synchronizing rock clocks of Earth history. *Science*, *320*(5875), 500–504. https://doi.org/10.1126/science.1154339

Laj, C., & Channell, J. E. (2015). Geomagnetic excursions. In G. Schubert & M. Kono (Eds.), *Treatise in geophysics, Geomagnetism* (Vol. 5, pp. 343–386).

Lawley, E. A. (1970). The intensity of the geomagnetic field in Iceland during Neogene polarity transitions and systematic deviations. *Earth and Planetary Science Letters*, *10*(1), 145–149. https://doi.org/10.1016/0012-821x(70)90076-2

Leonhardt, R., & Fabian, K. (2007). Paleomagnetic reconstruction of the global geomagnetic field evolution during the Matuyama/Brunhes transition: Iterative Bayesian inversion and independent verification. *Earth and Planetary Science Letters*, *253*(1–2), 172–195. https://doi.org/10.1016/j.epsl.2006.10.025

Leonhardt, R., McWilliams, M., Heider, F., & Soffel, H. (2009). The Gilsá excursion and the Matuyama/Brunhes transition recorded in $^{40}Ar/^{39}Ar$ dated lavas from Lanai and Maui, Hawaiian Islands. *Geophysical Journal International*, *179*(1), 43–58. https://doi.org/10.1111/j.1365-246x.2009.04264.x

Lund, S. P., & Keigwin, L. (1994). Measurement of the degree of smoothing in sediment paleomagnetic secular variation records: An example from late quaternary deep-sea sediments of the Bermuda rise, western North Atlantic Ocean. *Earth and Planetary Science Letters*, *122*(3–4), 317–330. https://doi.org/10.1016/0012-821x(94)90005-1

Macrì, P., Capraro, L., Ferretti, P., & Scarponi, D. (2018). A high-resolution record of the Matuyama-Brunhes transition from the Mediterranean region: The Valle di Manche section (Calabria, Southern Italy). *Physics of the Earth and Planetary Interiors*, *278*, 1–15. https://doi.org/10.1016/j.pepi.2018.02.005

Macrì, P., Sagnotti, L., Dinarès-Turell, J., & Caburlotto, A. (2005). A composite record of Late Pleistocene relative geomagnetic paleointensity from the Wilkes Land Basin (Antarctica). *Physics of the Earth and Planetary Interiors*, *151*(3–4), 223–242. https://doi.org/10.1016/j.pepi.2005.03.004

Macrì, P., Sagnotti, L., Dinarès-Turell, J., & Caburlotto, A. (2010). Relative geomagnetic paleointensity of the Brunhes Chron and the Matuyama–Brunhes precursor as recorded in sediment core from Wilkes Land Basin (Antarctica). *Physics of the Earth and Planetary Interiors*, *179*(1–2), 72–86. https://doi.org/10.1016/j.pepi.2009.12.002

Maegakiuchi, K., Hyodo, M., Kitaba, I., Hirose, K., Katoh, S., & Sato, H. (2016). Brief sea-level fall event and centennial to millennial sea-level variations during Marine Isotope Stage 19 in Osaka Bay, Japan. *Journal of Quaternary Science*, *31*(7), 809–822. https://doi.org/10.1002/jqs.2907

Maenaka, K. (1983). *Magnetostratigraphic study on the Osaka Group, with special reference to the existence of pre-and post-Jaramillo episodes in the late Matuyama polarity epoch* (Vol. 14, pp. 1–65). Mem. Hanazono University.

Mahgoub, A. N., Korte, M., & Panovska, S. (2023). Characteristics of the Matuyama-Brunhes magnetic field reversal based on a global data compilation. *Journal of Geophysical Research: Solid Earth*, *128*(2), e2022JB025286. https://doi.org/10.1029/2022jb025286

Mazaud, A., Channell, J. E. T., & Stoner, J. S. (2012). Relative paleointensity and environmental magnetism since 1.2 Ma at IODP site U1305 (Eirik drift, NW Atlantic). *Earth and Planetary Science Letters*, *357*, 137–144. https://doi.org/10.1016/j.epsl.2012.09.037

Mazaud, A., Channell, J. E. T., & Stoner, J. S. (2015). The paleomagnetic record at IODP Site U1307 back to 2.2 Ma (Eirik Drift, off south Greenland). *Earth and Planetary Science Letters*, *429*, 82–89. https://doi.org/10.1016/j.epsl.2015.07.059

Merrill, R. T., & McFadden, P. L. (1999). Geomagnetic polarity transitions. *Reviews of Geophysics*, *37*(2), 201–226. https://doi.org/10.1029/1998rg900004

Meynadier, L., Valet, J.-P., Bassinot, F. C., Shackleton, N. J., & Guyodo, Y. (1994). Asymmetrical saw-tooth pattern of the geomagnetic field intensity from equatorial sediments in the Pacific and Indian Oceans. *Earth and Planetary Science Letters*, *126*(1–3), 109–127. https://doi.org/10.1016/0012-821x(94)90245-3

Néel, L. (1955). Some theoretical aspects of rock-magnetism. *Advances in Physics*, *4*(14), 191–243. https://doi.org/10.1080/00018735500101204

Nowaczyk, N. R., Haltia, E., Ulbricht, D., Wennrich, V., Sauerbrey, M., Rosén, P., et al. (2013). Chronology of Lake El'gygytgyn sediments–a combined magnetostratigraphic, palaeoclimatic and orbital tuning study based on multi-parameter analyses. *Climate of the Past*, *9*(6), 2413–2432. https://doi.org/10.5194/cp-9-2413-2013

Oda, H., Nakazato, H., Nanayama, F., & Harigane, Y. (2022). Matuyama–Brunhes geomagnetic reversal record and associated key tephra layers in Boso Peninsula: Extraction of primary magnetization of geomagnetic fields from mixed magnetic minerals of depositional, diagenesis, and weathering processes. *Earth Planets and Space*, *74*(1), 1–29. https://doi.org/10.1186/s40623-022-01626-1

Oda, H., Shibuya, H., & Hsu, V. (2000). Palaeomagnetic records of the Brunhes/Matuyama polarity transition from ODP Leg 124 (Celebes and Sulu seas). *Geophysical Journal International*, *142*(2), 319–338. https://doi.org/10.1046/j.1365-246x.2000.00130.x

Olson, P. L., Glatzmaier, G. A., & Coe, R. S. (2011). Complex polarity reversals in a geodynamo model. *Earth and Planetary Science Letters*, *304*(1–2), 168–179. https://doi.org/10.1016/j.epsl.2011.01.031

Panovska, S., & Constable, C. (2017). An activity index for geomagnetic paleosecular variation, excursions, and reversals. *Geochemistry, Geophysics, Geosystems*, *18*(4), 1366–1375. https://doi.org/10.1002/2016gc006668

Panovska, S., Constable, C., & Brown, M. (2018). Global and regional assessments of paleosecular variation activity over the past 100 ka. *Geochemistry, Geophysics, Geosystems*, *19*(5), 1559–1580. https://doi.org/10.1029/2017gc007271

Panovska, S., Finlay, C. C., Donadini, F., & Hirt, A. M. (2012). Spline analysis of Holocene sediment magnetic records: Uncertainty estimates for field modeling. *Journal of Geophysical Research*, *117*(B2), B02101. https://doi.org/10.1029/2011jb008813

Panovska, S., Korte, M., Liu, J., & Nowaczyk, N. (2021). Global evolution and dynamics of the geomagnetic field in the 15–70 Kyr period based on selected paleomagnetic sediment records. *Journal of Geophysical Research: Solid Earth*, *126*(12), e2021JB022681. https://doi.org/10.1029/2021jb022681

Raisbeck, G., Yiou, F., Cattani, O., & Jouzel, J. (2006). ^{10}Be evidence for the Matuyama–Brunhes geomagnetic reversal in the EPICA Dome C ice core. *Nature*, *444*(7115), 82–84. https://doi.org/10.1038/nature05266

Roberts, A. P. (2008). Geomagnetic excursions: Knowns and unknowns. *Geophysical Research Letters*, *35*(17), L17307. https://doi.org/10.1029/2008gl034719

Roberts, A. P., & Winklhofer, M. (2004). Why are geomagnetic excursions not always recorded in sediments? Constraints from post-depositional remanent magnetization lock-in modelling. *Earth and Planetary Science Letters*, *227*(3–4), 345–359. https://doi.org/10.1016/j.epsl.2004.07.040

Sagnotti, L., Budillon, F., Dinarès-Turell, J., Iorio, M., & Macrì, P. (2005). Evidence for a variable paleomagnetic lock-in depth in the Holocene sequence from the Salerno Gulf (Italy): Implications for "high-resolution" paleomagnetic dating. *Geochemistry, Geophysics, Geosystems*, *6*(11), Q11013. https://doi.org/10.1029/2005gc001043

Sagnotti, L., Giaccio, B., Liddicoat, J. C., Nomade, S., Renne, P. R., Scardia, G., & Sprain, C. J. (2016). How fast was the Matuyama–Brunhes geomagnetic reversal? A new subcentennial record from the Sulmona Basin, central Italy. *Geophysical Journal International*, *204*(2), 798–812. https://doi.org/10.1093/gji/ggv486

Sagnotti, L., Scardia, G., Giaccio, B., Liddicoat, J. C., Nomade, S., Renne, P. R., & Sprain, C. J. (2014). Extremely rapid directional change during Matuyama-Brunhes geomagnetic polarity reversal. *Geophysical Journal International*, *199*(2), 1110–1124. https://doi.org/10.1093/gji/ggu287

Sato, T., Kikuchi, H., Nakashizuka, M., & Okada, M. (1998). Quaternary geomagnetic field intensity: Constant periodicity or variable period? *Geophysical Research Letters*, *25*(12), 2221–2224. https://doi.org/10.1029/98gl01621

Sato, T., & Kobayashi, K. (1989). Long-period secular variations of the Earth's magnetic field revealed by Pacific deep-sea sediment cores. *Journal of Geomagnetism and Geoelectricity*, *41*(1), 147–159. https://doi.org/10.5636/jgg.41.147

Shackleton, N., Berger, A., & Peltier, W. (1990). An alternative astronomical calibration of the lower Pleistocene timescale based on ODP Site 677. *Earth and Environmental Science Transactions of the Royal Society of Edinburgh*, *81*(4), 251–261. https://doi.org/10.1017/s0263593300020782

Shao, J.-C., Fuller, M., Tanimoto, T., Dunn, J., & Stone, D. (1999). Spherical harmonic analyses of paleomagnetic data: The time-averaged geomagnetic field for the past 5 Myr and the Brunhes-Matuyama reversal. *Journal of Geophysical Research*, *104*(B3), 5015–5030. https://doi.org/10.1029/98jb01354

Shin, J. Y., Yu, Y., & Kim, W. (2019). Wavelet-based verification of a relative paleointensity record from the North Pacific. *Earth Planets and Space*, *71*(1), 1–14. https://doi.org/10.1186/s40623-019-1067-x

Singer, B. S. (2014). A Quaternary geomagnetic instability time scale. *Quaternary Geochronology*, *21*, 29–52. https://doi.org/10.1016/j.quageo.2013.10.003

Singer, B. S., Hoffman, K. A., Chauvin, A., Coe, R. S., & Pringle, M. S. (1999). Dating transitionally magnetized lavas of the late Matuyama Chron: Toward a new ^{40}Ar/^{39}Ar timescale of reversals and events. *Journal of Geophysical Research*, *104*(B1), 679–693. https://doi.org/10.1029/1998jb900016

Singer, B. S., Hoffman, K. A., Coe, R. S., Brown, L. L., Jicha, B. R., Pringle, M. S., & Chauvin, A. (2005). Structural and temporal requirements for geomagnetic field reversal deduced from lava flows. *Nature*, *434*(7033), 633–636. https://doi.org/10.1038/nature03431

Singer, B. S., Jicha, B. R., Mochizuki, N., & Coe, R. S. (2019). Synchronizing volcanic, sedimentary, and ice core records of Earth's last magnetic polarity reversal. *Science Advances*, *5*(8), eaaw4621. https://doi.org/10.1126/sciadv.aaw4621

Suganuma, Y., Okada, M., Horie, K., Kaiden, H., Takehara, M., Senda, R., et al. (2015). Age of Matuyama-Brunhes boundary constrained by U-Pb zircon dating of a widespread tephra. *Geology*, *43*(6), 491–494. https://doi.org/10.1130/g36625.1

Suttie, N., & Nilsson, A. (2019). Archaeomagnetic data: The propagation of an error. *Physics of the Earth and Planetary Interiors*, *289*, 73–74. https://doi.org/10.1016/j.pepi.2019.02.008

Valet, J.-P., Bassinot, F., Bouilloux, A., Bourlès, D., Nomade, S., Guillou, V., et al. (2014). Geomagnetic, cosmogenic and climatic changes across the last geomagnetic reversal from Equatorial Indian Ocean sediments. *Earth and Planetary Science Letters*, *397*, 67–79. https://doi.org/10.1016/j.epsl.2014.03.053

Valet, J.-P., Bassinot, F., Simon, Q., Savranskaia, T., Thouveny, N., Bourlés, D. L., & Villedieu, A. (2019). Constraining the age of the last geomagnetic reversal from geochemical and magnetic analyses of Atlantic, Indian, and Pacific Ocean sediments. *Earth and Planetary Science Letters*, *506*, 323–331. https://doi.org/10.1016/j.epsl.2018.11.012

Valet, J.-P., & Fournier, A. (2016). Deciphering records of geomagnetic reversals. *Reviews of Geophysics*, *54*(2), 410–446. https://doi.org/10.1002/2015rg000506

Valet, J.-P., Fournier, A., Courtillot, V., & Herrero-Bervera, E. (2012). Dynamical similarity of geomagnetic field reversals. *Nature*, *490*(7418), 89–93. https://doi.org/10.1038/nature11491

Valet, J.-P., & Meynadier, L. (1993). Geomagnetic field intensity and reversals during the past four million years. *Nature*, *366*(6452), 234–238. https://doi.org/10.1038/366234a0

Valet, J.-P., Meynadier, L., Simon, Q., & Thouveny, N. (2016). When and why sediments fail to record the geomagnetic field during polarity reversals. *Earth and Planetary Science Letters*, *453*, 96–107. https://doi.org/10.1016/j.epsl.2016.07.055

Van Zijl, J., Graham, K., & Hales, A. (1962). The palaeomagnetism of the Stormberg Lavas, II. The behaviour of the magnetic field during a reversal. *Geophysical Journal of the Royal Astronomical Society*, *7*(2), 169–182. https://doi.org/10.1111/j.1365-246x.1962.tb00366.x

Verosub, K. L., & Banerjee, S. K. (1977). Geomagnetic excursions and their paleomagnetic record. *Reviews of Geophysics*, *15*(2), 145–155. https://doi.org/10.1029/rg015i002p00145

Wang, D., Wang, Y., Han, J., Duan, M., Shan, J., & Liu, T. (2010). Geomagnetic anomalies recorded in L9 of the Songjiadian loess section in southeastern Chinese Loess Plateau. *Chinese Science Bulletin*, *55*(6), 520–529. https://doi.org/10.1007/s11434-009-0565-9

Whaler, K., & Gubbins, D. (1981). Spherical harmonic analysis of the geomagnetic field: An example of a linear inverse problem. *Geophysical Journal International*, *65*(3), 645–693. https://doi.org/10.1111/j.1365-246x.1981.tb04877.x

Xuan, C., Channell, J. E. T., & Hodell, D. A. (2016). Quaternary magnetic and oxygen isotope stratigraphy in diatom-rich sediments of the southern Gardar Drift (IODP Site U1304, North Atlantic). *Quaternary Science Reviews*, *142*, 74–89. https://doi.org/10.1016/j.quascirev.2016.04.010

Yamazaki, T., & Kanamatsu, T. (2007). A relative paleointensity record of the geomagnetic field since 1.6 Ma from the North Pacific. *Earth Planets and Space*, *59*(7), 785–794. https://doi.org/10.1186/bf03352741

Yamazaki, T., & Oda, H. (2005). A geomagnetic paleointensity stack between 0.8 and 3.0 Ma from equatorial Pacific sediment cores. *Geochemistry, Geophysics, Geosystems*, *6*(11), Q11H20. https://doi.org/10.1029/2005gc001001

Yang, T., Hyodo, M., Yang, Z., & Fu, J. (2004). Evidence for the Kamikatsura and Santa Rosa excursions recorded in eolian deposits from the southern Chinese Loess Plateau. *Journal of Geophysical Research*, *109*(B12), B12105. https://doi.org/10.1029/2004jb002966

Ziegler, L., Constable, C., Johnson, C., & Tauxe, L. (2011). PADM2M: A penalized maximum likelihood model of the 0–2 Ma palaeomagnetic axial dipole moment. *Geophysical Journal International*, *184*(3), 1069–1089. https://doi.org/10.1111/j.1365-246x.2010.04905.x